Bidirectional genome-wide CRISPR screens reveal host factors regulating SARS-CoV-2, MERS-CoV and seasonal HCoVs

Caroline Goujon (caroline.goujon@irim.cnrs.fr)
French National Centre for Scientific Research, Montpellier university https://orcid.org/0000-0001-8571-1108

Antoine Rebendenne
French National Centre for Scientific Research, Montpellier university

Priyanka Roy
Genetic Perturbation Platform, Broad Institute of MIT and Harvard

Boris Bonaventure
French National Centre for Scientific Research, Montpellier university

Ana Chaves Valadao
French National Centre for Scientific Research, Montpellier university

Lowiese Desmarets
Lille University, CNRS, INSERM, CHU Lille, Institut Pasteur de Lille https://orcid.org/0000-0001-5077-3333

Yves Rouillé
Lille University, CNRS, INSERM, CHU Lille, Institut Pasteur de Lille

Marine Tauziet
French National Centre for Scientific Research, Montpellier university

Mary Arnaud-Arnould
French National Centre for Scientific Research, Montpellier university https://orcid.org/0000-0003-2799-1011

Donatella Giovannini
French National Centre for Scientific Research, Montpellier university

Yenarae Lee
Broad Institute of MIT and Harvard

Peter DeWeirdt
Broad Institute

Mudra Hegde
Broad Institute https://orcid.org/0000-0003-4530-4633

Francisco Garcia de Gracia
French National Centre for Scientific Research, Montpellier university

Joe McKellar
French National Centre for Scientific Research, Montpellier university
Mélanie Wencker
INSERM, ENS-Lyon, Lyon University
Jean Dubuisson
Lille University, CNRS, INSERM, CHU Lille, Institut Pasteur de Lille
Sandrine Belouzard
Lille University, CNRS, INSERM, CHU Lille, Institut Pasteur de Lille
Olivier Moncorgé
French National Centre for Scientific Research, Montpellier university
John Doench
Broad Institute https://orcid.org/0000-0002-3707-9889

Article

Keywords: TMPRSS2, Plasma Membrane, Calu-3 Lung Epithelial Cells, AP1G1, AP1B1, ATP8B1, IL6R, CD44, Viral Entry, Adaptins, Flippase, Mucins

DOI: https://doi.org/10.21203/rs.3.rs-555275/v1

Bidirectional genome-wide CRISPR screens reveal host factors regulating SARS-CoV-2, MERS-CoV and seasonal HCoVs

Rebendenne Antoine[1], Roy Priyanka[2], Bonaventure Boris[1*], Chaves Valadão Ana Luiza[1*], Desmarets Lowiese[3], Rouillé Yves[3], Tauziet Marine[1], Arnaud-Arnould Mary[1], Giovannini Donatella[4,5], Lee Yenarae[2], DeWeirdt Peter[2], Hegde Mudra[2], Garcia de Gracia Francisco[1], McKellar Joe[1], Wencker Mélanie[6], Dubuisson Jean[3], Belouzard Sandrine[3], Moncorgé Olivier[1], Doench John G.[2§], and Goujon Caroline[1§]

[1] IRIM, CNRS, Montpellier University, France

[2] Genetic Perturbation Platform, Broad Institute of MIT and Harvard, Cambridge, USA

[3] Lille University, CNRS, INSERM, CHU Lille, Institut Pasteur de Lille, France

[4] IGMM, CNRS, Montpellier University, France

[5] Metafora Biosystems, Paris, France

[6] CIRI, INSERM, CNRS, ENS-Lyon, Lyon University, France

* Equal contributions; § corresponding authors

Abstract

Several genome-wide CRISPR knockout screens have been conducted to identify host factors regulating SARS-CoV-2 replication, but the models used have often relied on overexpression of ACE2 receptor. Additionally, such screens have yet to identify the protease TMPRSS2, known to be important for viral entry at the plasma membrane. Here, we conducted a meta-analysis of these screens and showed a high level of cell-type specificity of the identified hits, arguing for the necessity of additional models to uncover the full landscape of SARS-CoV-2 host factors. We performed genome-wide knockout and activation CRISPR screens in Calu-3 lung epithelial cells, as well as knockout

screens in Caco-2 intestinal cells. In addition to identifying ACE2 and TMPRSS2 as top hits, our study reveals a series of so far unidentified and critical host-dependency factors, including the Adaptins AP1G1 and AP1B1 and the flippase ATP8B1. Moreover, new anti-SARS-CoV-2 proteins with potent activity, including several membrane-associated Mucins, IL6R, and CD44 were identified. We further observed that these genes mostly acted at the critical step of viral entry, with the notable exception of ATP8B1, the knockout of which prevented late stages of viral replication. Exploring the pro- and anti-viral breadth of these genes using highly pathogenic MERS-CoV, seasonal HCoV-NL63 and -229E and influenza A orthomyxovirus, we reveal that some genes such as AP1G1 and ATP8B1 are general coronavirus cofactors. In contrast, Mucins recapitulated their known role as a general antiviral defense mechanism. These results demonstrate the value of considering multiple cell models and perturbational modalities for understanding SARS-CoV-2 replication and provide a list of potential new targets for therapeutic interventions.

Introduction

Severe acute respiratory syndrome coronavirus 2 (SARS-CoV-2) is the etiologic agent of the coronavirus disease 2019 (COVID-19) pandemic, which has been applying an unprecedented pressure on health systems worldwide since it was first detected in China at the end of 2019. As of today (May 23, 2021), SARS-CoV-2 continues to spread worldwide, with over 167 million confirmed cases and >3,4 million deaths.

SARS-CoV-2 is the third highly pathogenic coronavirus to cross the species barrier in the 21st century and cause an epidemic in the human population after SARS-CoV(-1) in 2002-2003 [1–3] and Middle East respiratory syndrome (MERS)-CoV in 2012 [4]. These three coronaviruses share some common clinical features, including breathing difficulty, acute respiratory distress syndrome (ARDS) and death in the most extreme cases [5]. Four additional Human Coronaviruses (HCoV-229E, -NL63, -OC43 and -HKU1) are known to circulate seasonally in humans and are associated with multiple respiratory diseases of

varying severity including common cold, pneumonia and bronchitis, contributing to approximately one-third of common cold infections in humans [6].

Coronaviruses are enveloped, positive stranded RNA viruses with a genome of approximately 30 kilobases. Highly pathogenic SARS-CoV-1, MERS-CoV and SARS-CoV-2, as well as seasonal HCoV-OC43 and HCoV-HKU1, belong to the genus *betacoronavirus,* whereas seasonal HCoV-229E and HCoV-NL63 are alphacoronaviruses. The respiratory tract is the main replication site of SARS-CoV-2, but it has also been shown to replicate in the gastrointestinal tract [7] and infect other cell types. Like SARS-CoV-1 and HCoV-NL63, SARS-CoV-2 entry into target cells is mediated by the Angiotensin converting enzyme 2 (ACE2) receptor [8–12]. The cellular serine protease Transmembrane protease, serine 2 (TMPRSS2) is employed by both SARS-CoV-1 and -2 for Spike (S) protein priming at the plasma membrane [8,13]. Cathepsins are also involved in SARS-CoV S protein cleavage and fusion peptide exposure upon entry via an endocytic route in the absence of TMPRSS2 [14–16]. HCoV-229E entry into target cells is mediated by membrane aminopeptidase N (ANPEP) [17], whereas MERS-CoV enters via dipeptidyl peptidase 4 (DPP4) [18]. Importantly, both these coronaviruses are also known to use TMPRSS2 for S protein activation [19,20].

Following viral entry and delivery of the viral genomic RNA associated with the nucleocapsid (N) to the cytoplasm, ORF1a/b is directly accessible to the translation machinery, which leads to the synthesis of two polyproteins (pp), pp1a and pp1b. These polyproteins are further processed into nonstructural proteins, which are important for the formation of replication and transcription complexes. The replication/transcription steps take place at the endoplasmic reticulum (ER) through the active formation of replication organelles surrounded by double membranes, which form a protective microenvironment against viral sensors and restriction factors. Subgenomic RNAs are then transcribed, translated into structural proteins, and translocated to the ER. The assembly takes place at the endoplasmic reticulum-Golgi intermediate compartments, where newly produced

genomic RNAs associated with N are also recruited. Budding occurs at the Golgi compartment and newly generated virions are released by exocytosis (reviewed in [21]).

Coronaviruses, which are found throughout the animal kingdom with an important diversity in bats, have a particularly high potential for cross-species transmission and may be the origin of future pandemics [22]. There is therefore a dire need to study coronaviruses in depth and to identify new therapeutic targets against these viruses.

Several whole-genome knockout (KO) CRISPR screens for the identification of coronavirus regulators have been recently reported [23–28]. These screens used simian Vero E6 cells [27], human Huh7 cells (or derivatives) ectopically expressing ACE2 and TMPRSS2 or not [23,25,26], and A549 cells ectopically expressing ACE2 [24,28]. Here, we conducted genome-wide loss-of-function screens by CRISPR knockout (KO) and gain-of-function screens by CRISPR activation (CRISPRa) to identify host factors modulating SARS-CoV-2 infection. Naturally permissive simian Vero E6 cells, as well as physiologically relevant human lung epithelial Calu-3 cells and intestinal Caco-2 cells, were used in these screens. Well-known SARS-CoV-2 host dependency factors were identified as top hits, such as ACE2, and either TMPRSS2 or Cathepsin L (depending on the cell type), validating the rationale of this study. Moreover, ACE2 scored as the top enriched and top depleted hit in all CRISPR KO and CRISPRa screens in Calu-3 cells, respectively, underlying the complementarity of both approaches. We validated the role of our top hits using individual CRISPR KO or activation in Calu-3 cells and assessed their effect on other coronaviruses and orthomyxovirus influenza A. Altogether, this quantitative and integrative study provides new insights in SARS-CoV-2 life cycle by identifying new host factors that modulate either positively or negatively replication of SARS-CoV-2 and other coronaviruses, and might lead to new, pan-coronavirus strategies for host-directed therapies.

118 **Results**

119

120 Meta-analysis of existing CRISPR KO screen data highlights the importance of diverse
121 models

122 African Green Monkey (*Chlorocebus sabaeus*) Vero E6 cells of kidney origin are
123 commonly used to amplify SARS-CoV-2 and present high levels of cytopathic effects
124 (CPE) upon replication, making them ideal to perform whole-genome CRISPR screens
125 for host factor identification. A *C. sabaeus* sgRNA library was previously described and
126 successfully used to identify host factors regulating SARS-CoV-2 (isolate USA-
127 WA1/2020) and other coronavirus replication [27]. In order to determine whether hit
128 identification based on whole-genome CRISPR screens was reproducible across different
129 laboratories and virus isolates, we initially repeated whole-genome CRISPR KO screens
130 in Vero E6 cells using the SARS-CoV-2 isolate BetaCoV/France/IDF0372/2020. Vero E6
131 cells were first stably engineered to express Cas9 and activity was validated with a GFP
132 activity assay. We then transduced the cells with the *C. sabaeus* genome-wide pooled
133 CRISPR library [27] at a low MOI (~0.1-0.5) in biological duplicates, the first of which was
134 then divided into three technical replicates. Cells were either collected for subsequent
135 genomic DNA extraction or challenged with SARS-CoV-2 at MOI 0.005, a viral input that
136 induced cell death in >95% of the cells in 3-4 days. After viral challenge, surviving cells
137 were propagated for 11-13 days to increase cell numbers prior to genomic DNA
138 extraction, PCR, and Illumina sequencing (**Fig. 1a**). We determined the log2-fold-change
139 (LFC) of guides, comparing SARS-CoV-2-challenged to untreated cells, and observed
140 that replicates for these screens were well-correlated (**Fig. S1a**).

141

142 We first examined the results from this screen and saw that ACE2 was a top hit, among
143 other genes (**Fig. 1b**). Compared to the prior results from the Wilen lab, this screen
144 showed greater statistical significance for proviral (resistance) hits, indicating that the
145 screening conditions employed here resulted in stronger selective pressure (**Fig. 1c**, **Fig.
146 S1b**). Nevertheless, proviral hits were consistent across the two screens, with 11 genes
147 scoring in the top 20 of both datasets, including ACE2 and CTSL; similarly, 6 of the top

20 anti-viral (sensitization) hits were in common, including HIRA and CABIN1, both members of an H3.3 specific chaperone complex.

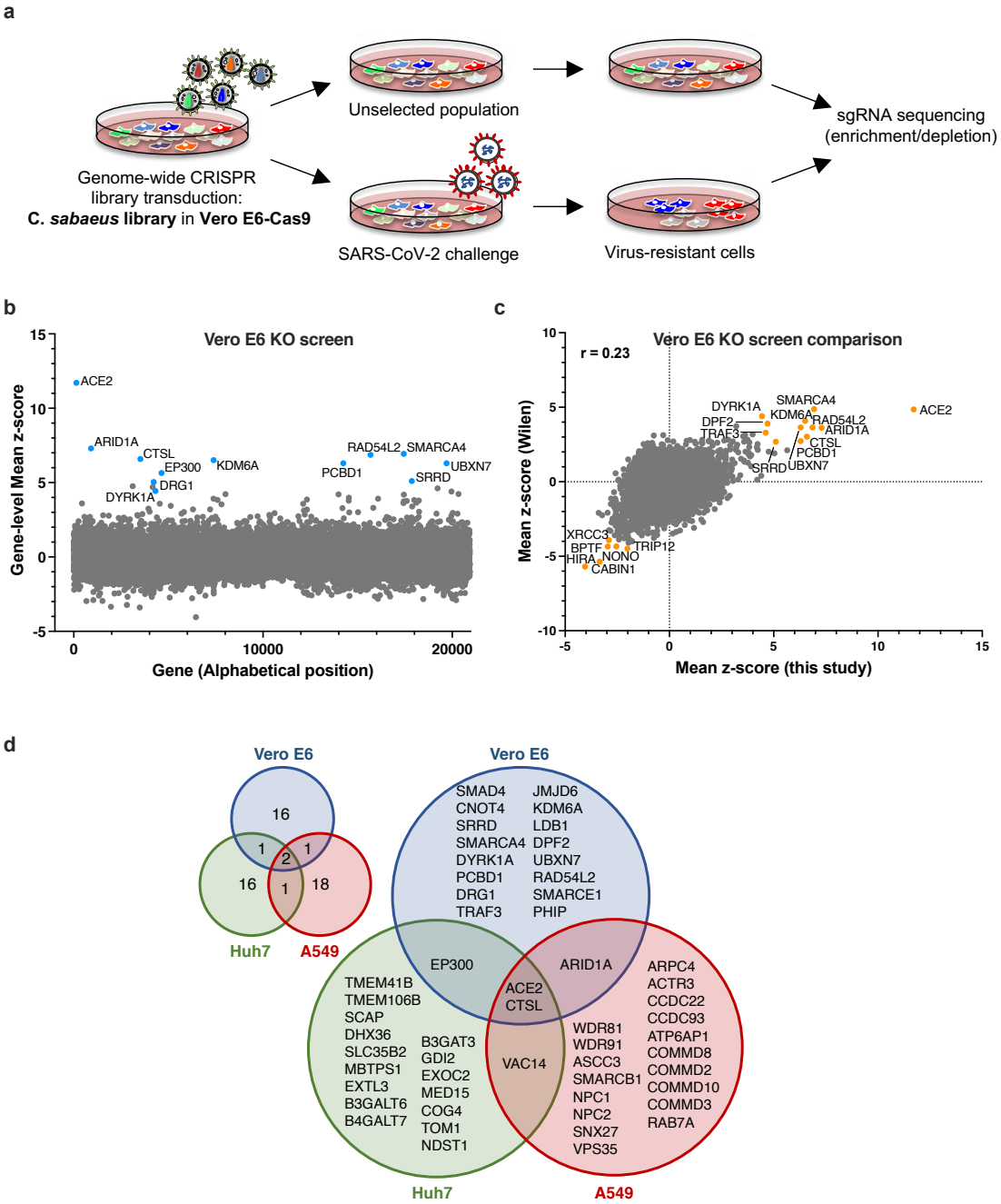

Fig. 1. Cell-type specificity of SARS-CoV-2 regulators identified by CRISPR screens.
a. Schematic of pooled screen to identify SARS-CoV-2 regulators in Vero E6 cells.
b. Scatter plot showing the gene-level mean z-scores of genes when knocked out in Vero E6 cells. The top genes conferring resistance to SARS-CoV-2 are annotated and shown in blue.
c. Comparison between this Vero E6 screen to the Vero E6 screen conducted by the Wilen lab [27]. Genes that scored among the top 20 resistance hits and sensitization hits in both screens are labeled.

157 **d.** Venn diagram comparing hits across screens conducted in Vero E6, A549, and Huh7 (or derivatives)
158 cells (ectopically expressing ACE2 and TMPRSS2 or not) [23–28]. The top 20 genes from each cell line are
159 included, with genes considered a hit in another cell line if the average z-score was > 3.
160
161 The additional, recently published genome-wide screens for SARS-CoV-2 host factors
162 have varied in the viral isolate, the CRISPR library, and the cell type (**Table 1**) [23–28]. We
163 acquired the read counts from all these screens and re-processed the data via the same
164 analysis pipeline to enable fair comparisons (see Methods); top-scoring genes were
165 consistent with the analyses provided in the original publications. Two screens, using
166 different CRISPR libraries, were conducted in A549 cells engineered to express ACE2;
167 comparison of these results showed a greater number of statistically significant hits in the
168 Zhang-Brunello dataset [28] compared to the Sanjana-GeCKO dataset [24], but results were
169 generally consistent between the two, with 10 genes shared in the top 20 (**Fig. S1c**).
170 Likewise, three groups conducted survival screens in related cell systems (**Fig. S1d)**:
171 Huh7 cells (Daelemans-Brunello [23]); Huh7.5 cells (Poirier-Brunello [25]), a derivative of
172 Huh7, which have biallelic loss-of-function mutation in the DDX58/RIG-I sensor; and
173 Huh7.5.1 cells, engineered to overexpress ACE2 and TMPRSS2 (Puschnik-GeCKO [26]).
174 All three screens identified TMEM106B as a top hit, and we observed the best pair-wise
175 correlation between the two screens that used Huh7.5 and Huh7.5.1 cells (**Fig. S1d**).
176
177 We next averaged gene-level z-scores and compared results across the Vero E6, A549,
178 and Huh7 cell lines. Examining the top 20 genes from each cell line, and using a lenient
179 z-score threshold of 3 to consider a gene a hit, we generated a Venn diagram to examine
180 their overlap (**Fig. 1d**). By these criteria, only ACE2 and CTSL scored in all three models,
181 and 3 additional genes overlapped in two cell lines. Examining the cell-line specific hits,
182 in Vero E6 cells we continued to observe an enrichment of BAF proteins SMARCA4 and
183 DPF2 (Wei et al., 2021); notably, another nBAF complex member, ARID1A, also scored
184 in A549 cells. Genes scoring uniquely in A549 cells included several COMM domain-
185 containing proteins, which have been implicated in NF-κB signaling [29]. Finally, Huh7 cells
186 showed specificity for EXT1 and EXT3L, genes involved in heparin sulfate biosynthesis,
187 as well as SLC35B2, which transports PAP, a substrate for intracellular sulfation. Overall,

these analyses suggest that individual cell models are particularly suited, in as yet unpredictable ways, to probe different aspects of SARS-CoV-2 host factor biology.

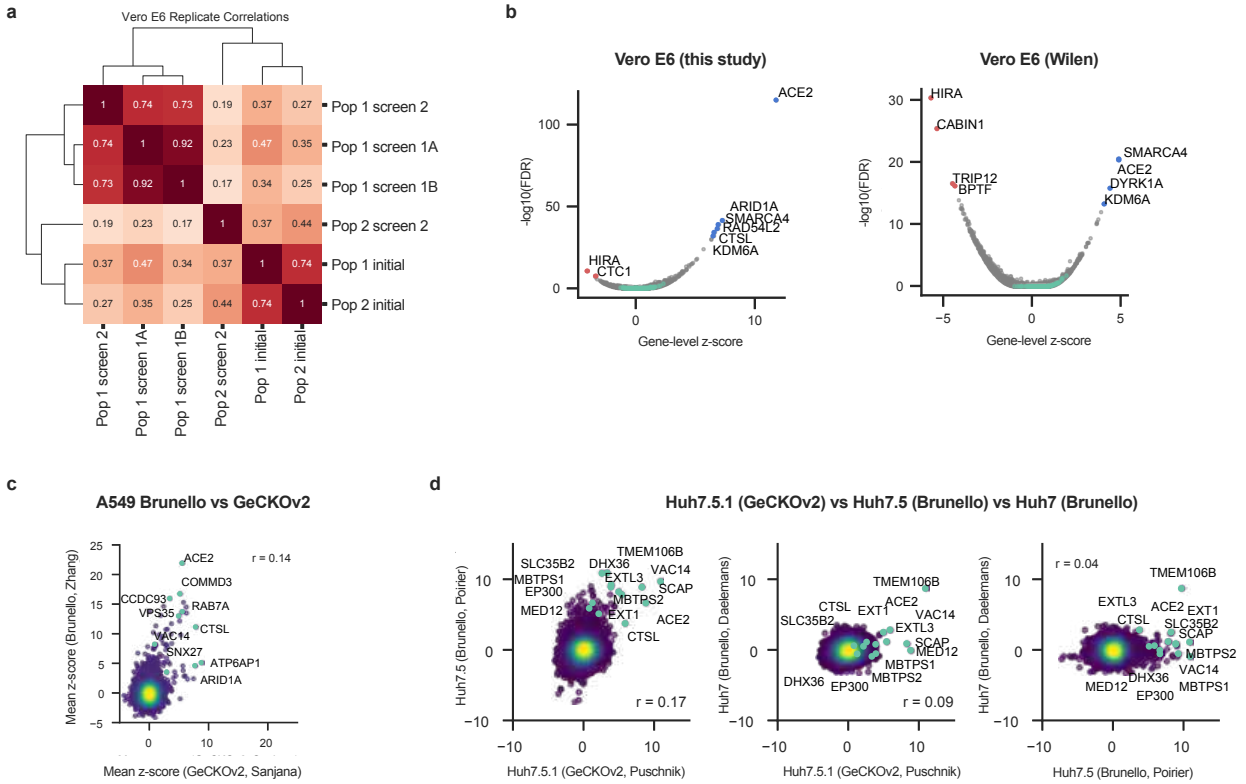

Fig. S1.

a. Clustermap showing correlations of log-fold change values relative to plasmid DNA across replicates in the Vero E6 screen from the present study. Population 1 (Pop 1) and Population 2 (Pop 2) refers to 2 independent library transductions, in which screens 1A, 1B and 2 refer to biological replicates of SARS-CoV-2 infection in Pop 1 and screen 2 refers to one biological replicate of SARS-CoV-2 infection in Pop 2. "Initial" refers to the uninfected condition.

b. Volcano plot showing the top genes conferring resistance (right, blue) and sensitivity (left, red) to SARS-CoV-2 when knocked out in Vero E6 cells for this screen and the screen conducted by Wei et al. 2021 (Wilen; [27]). The gene-level z-score and -log10(FDR) were calculated after averaging across conditions (of note, the FDR value for ACE2 is effectively zero but has been assigned a -log(FDR) value for plotting purposes).

c. Comparison between genome-wide screens conducted in A549 cells overexpressing ACE2 by Daniloski et al. (Sanjana; [24]) and Zhu et al. (Zhang; [28]) using the GeCKOv2 and Brunello libraries, respectively.

d. Pair-wise comparison between genome-wide screens conducted in Huh7.5.1-ACE2-TMPRSS2, Huh7.5, and Huh7 cells by Wang et al. (Puschnik; [26]), Schneider et al. (Poirier; [25]), and Baggen et al. (Daelemans; [23]), respectively, using the GeCKOv2 and Brunello libraries as indicated. Annotated genes include top 3 resistance hits from each screen as well as genes that scored in multiple cell lines based on the criteria used to construct the Venn diagram in **Fig. 1d**.

211 Whole-genome knockout and activation screens to identify genes regulating SARS-CoV-
212 2 replication in Calu-3 cells
213 Calu-3 cells, a lung adenocarcinoma cell line, are a particularly attractive model for
214 exploring SARS-CoV-2 biology, as they naturally express ACE2 and TMPRSS2.
215 Furthermore, we have previously shown that Calu-3 cells behave highly similarly to
216 primary human airway epithelia when challenged with SARS-CoV-2 [30]. Additionally, they
217 are suited to viability-based screens, as they are highly permissive to SARS-CoV-2 and
218 show high levels of cytopathic effects upon replication, although the slow doubling time
219 of the cells (~5-6 days) presents challenges for scale-up.
220
221 To conduct genome-wide CRISPR KO and activation screens (**Fig. 2a**), Calu-3 cells were
222 stably engineered to express Cas9 or dCas9-VP64, respectively. Calu-3-Cas9 cells
223 showed >94% Cas9 activity (**Fig. S2a**) and Calu-3-dCas9-VP64 cells transduced to
224 express sgRNAs targeting the *MX1* and *IFITM3* promoters induced expression to a similar
225 magnitude as following interferon treatment (**Fig. S2b-c**). The more compact Gattinara
226 library [31] was selected for the knockout screen due to the difficulty of scaling-up this cell
227 line, while the Calabrese library was used for the CRISPRa screen [32]. Cells were
228 transduced with the libraries in biological triplicates at a low MOI, selected with puromycin,
229 and 15 to 18 days post-transduction, were either harvested for subsequent genomic DNA
230 extraction or challenged with SARS-CoV-2 at MOI 0.005, which led to >90% cell death in
231 3-5 days. The surviving cells were then cultured in conditioned media, expanded and
232 harvested when cell numbers were sufficient for genomic DNA extraction (see Methods).
233 The screening samples were processed and analyzed as above.
234
235 The knockout screen was most powered to identify proviral factors (**Fig. S2d**), and the
236 top three genes were ACE2, KMT2C and TMPRSS2 (**Fig. 2b**). Importantly, the latter did
237 not score in any of the cell models discussed above; conversely, CTSL did not score in
238 this screen. Interestingly, whereas the BAF-specific ARID1A scored in Vero E6 cells and
239 A549 cells, PBAF-specific components ARID2 (rank 5) and PRBM1 (rank 7) scored as
240 top hits in Calu-3. Additional new hits include AP1G1 (rank 4), AP1B1 (rank 9), and

AAGAB (rank 22), which code for proteins involved in the formation of clathrin-coated pits and vesicles, and are important for vesicle-mediated, ligand-receptor complex intracellular trafficking.

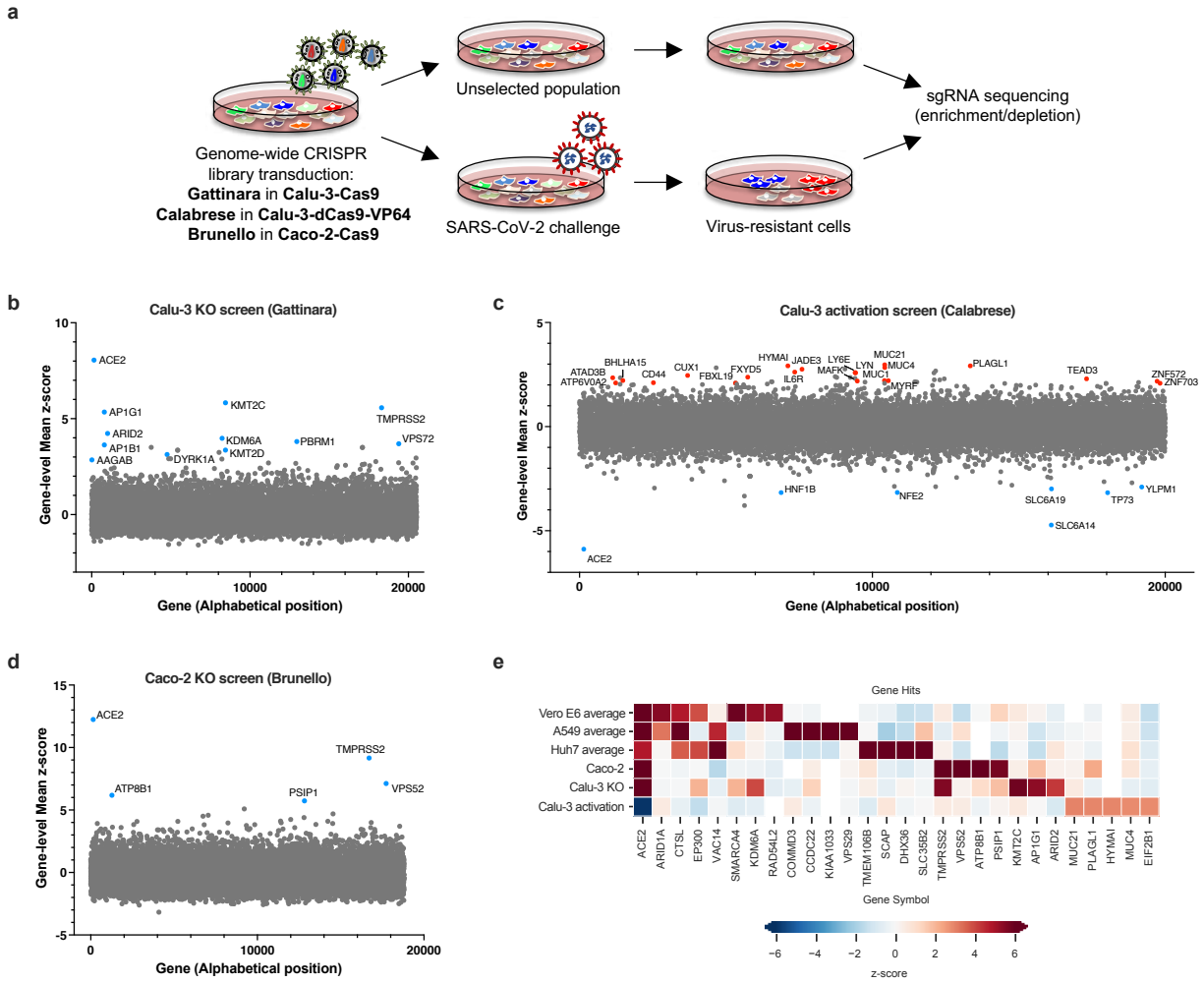

Fig. 2. Genome-wide CRISPR screens in Calu-3 reveal new regulators of SARS-CoV-2.
a. Schematic of pooled screens (Calu-3 KO/CRISPRa, Caco-2 KO).
b. Scatter plot showing the gene-level mean z-scores of genes when knocked out in Calu-3 cells. The top genes conferring resistance to SARS-CoV-2 are annotated and shown in blue. This screen did not have any sensitization hits.
c. Scatter plot showing the gene-level mean z-scores of genes when over-expressed in Calu-3 cells. The top genes conferring resistance to SARS-CoV-2 are annotated and shown in red. The top genes conferring sensitivity to SARS-CoV-2 are annotated and shown in blue.
d. Scatter plot showing the gene-level mean z-scores of genes when knocked out in Caco-2 cells. The top genes conferring resistance to SARS-CoV-2 are annotated and shown in blue.
e. Heatmap of top 5 resistance hits from each cell line after averaging across screens in addition to genes that scored in multiple cell lines based on the criteria used to construct the Venn diagram in Fig. 1D (based on [23–28] and this study).

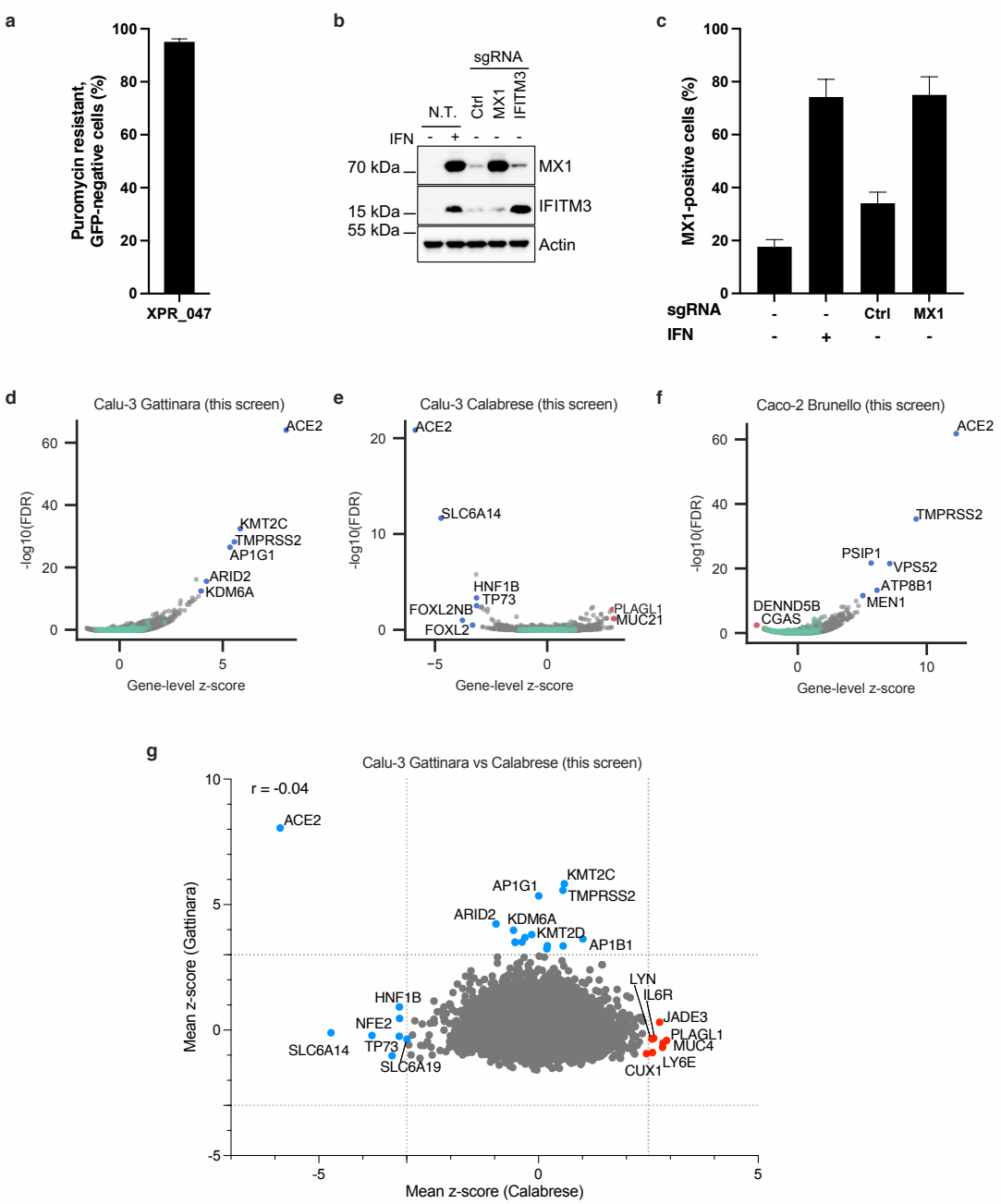

Fig. S2.

a. Calu-3 cells stably expressing Cas9 were transduced with a lentiviral vector expressing the puromycin resistance gene and GFP, as well as a sgRNA targeting the GFP coding sequence (XPR_047). The percentage of puromycin-resistant cells which did not express detectable levels of GFP was scored by flow cytometry 8-10 days post-transduction.

b. and **c.** Calu-3 cells stably expressing dCas9-VP64 were transduced or not with lentiviral vectors expressing sgRNAs targeting either nothing (Ctrl), *MX1* or *IFITM3* promoter and puromycin-selected for 8-10 days. In parallel, non-transduced (N.T.) cells were treated or not with 1000 U/mL interferon for 24h. Cells were harvested for immunoblot analysis (**b**) or fixed, permeabilized and stained with an anti-MX1 antibody and an Alexa Fluor 488 secondary antibody and analyzed by flow cytometry (**C**). Biological duplicates (**a, c**) and a representative immunoblot (**b**) are shown.

d. Volcano plot showing the top genes conferring resistance (right, blue) to SARS-CoV-2 when knocked out in Calu-3 cells. This screen did not have any sensitization hits. The gene-level z-score and -log10(FDR) were calculated after averaging across replicates.
e. Volcano plot showing the top genes conferring resistance (right, red) and sensitivity (left, blue) to SARS-CoV-2 when overexpressed in Calu-3 cells. The gene-level z-score and -log10(FDR) were calculated after averaging across replicates.
f. Volcano plot showing the top genes conferring resistance (right, blue) and sensitivity (left, red) to SARS-CoV-2 when knocked out in Caco-2 cells. The gene-level z-score and -log10(FDR) were calculated after averaging across replicates.
g. Comparison between gene hits in Calu-3 KO and activation screens. Dotted lines indicated mean z-scores of -3 and 2.5 or 3 for each screen. Proviral and antiviral genes are indicated in blue and red, respectively.

We next examined the CRISPRa screen (**Fig. 2c and S2e)**. In contrast to the knockout screen, here we were able to detect both pro- and anti-viral genes; we speculate this is due to the shorter length of time in culture post-SARS-challenge for the activation screens (2 weeks, compared to 4 in the knockout screens). Assuringly, the top-scoring proviral (sensitization) hit was ACE2. Several solute carrier (SLC) transport channels also scored on this side of the screen, including SLC6A19 (rank 8), which is a known partner of ACE2 [33]. Furthermore, SLC6A14 (rank 2) has been implicated in cystic fibrosis progression and shown to regulate the attachment of *Pseudomonas* to human bronchial epithelial cells [34]. On the antiviral side of the screen, a top scoring hit was LY6E (rank 10), which is a known restriction factor of SARS-CoV-2 [35], further validating the ability of this screening technology and cellular model to identify known biology. Additionally, MUC21 (rank 1), MUC4 (rank 4), and MUC1 (rank 26) all scored; Mucins are heavily glycosylated proteins and have a well-established role in host defense against pathogens [36,37]; moreover, MUC4 has been recently proposed to possess a protective role against SARS-CoV-1 pathogenesis in a mouse model [38]. Finally, we directly compared the knockout and activation screens conducted in Calu-3 cells (**Fig. S2g**). The only gene that scored in both the knockout and activation screen, even using a lenient z-score threshold of >3, was ACE2, emphasizing that different aspects of biology are revealed by these screening technologies.

To expand the range of cell lines examined further, we also performed a knockout screen with the Brunello library in another cell line naturally permissive to SARS-CoV-2 replication, the colorectal adenocarcinoma Caco-2 cell line. Here, however, the cells were

306 engineered to overexpress ACE2 in order to reach sufficient levels of CPE to enable
307 viability-based screening. Similar to Calu-3 cells, ACE2 and TMPRSS2 were the top
308 resistance hits (**Fig. 2d, S2d and S2f**), indicating that Caco-2 and Calu-3 cells, unlike
309 previously used models, rely on TMPRSS2-mediated cell entry, rather than the CTSL-
310 mediated endocytic pathway, which did not score in this cell line (z-score=-0.2).
311 Assembling all the proviral genes identified across 5 cell lines, we observed a continuation
312 of the trend that screen results are largely cell line dependent (**Fig. 2e**).
313

314 Individual validations via CRISPR KO confirm the identification of new proviral genes,
315 including members of the AP-1 complex

316 First we focused on the proviral genes identified in our KO screens and selected 22
317 candidates among the top ones identified in the screens performed in Calu-3, Vero E6
318 and Caco-2 cells. We designed 2 sgRNAs to target these genes and generated polyclonal
319 knockout Calu-3 cell populations. In parallel, we generated 2 negative control cell lines
320 (coding non-targeting sgRNAs) and 2 positive control cell lines (*ACE2* and *TMPRSS2*
321 KO*)*. Two weeks post-transduction, knockout cell lines were challenged with SARS-CoV-
322 2 bearing the mNeonGreen (mNG) reporter [39] and the percentage of infected cells was
323 scored by flow cytometry (**Fig. 3a**). The knockout of about half of the selected genes
324 induced at least a 50% decrease in infection efficiency. Among them, *AP1G1* KO had an
325 inhibitory effect as drastic as *ACE2* KO (>95% decrease in infection efficiency), showing
326 an absolutely essential role of this particular gene. Another member of the Adaptin family,
327 *AP1B1,* and a known partner of the AP-1 complex, *AAGAB*, also had an important impact,
328 albeit not as strong (~70-90% decrease in infection). The KO of 3 other genes *KMT2C*,
329 *EP300*, and *ATP8B1*, which code for a lysine methyltransferase, a histone acetyl
330 transferase and a flippase, respectively, inhibited the infection efficiency by at least 50%.
331 In parallel, we tested the impact of candidate knockout on SARS-CoV-2-induced CPEs.
332 Cells were infected with wild-type SARS-CoV-2 at an MOI of 0.005 and colored with
333 crystal violet when massive CPE was observed in the negative controls, ~5 days post-
334 infection (**Fig. S3a**). CPE analyses globally mirrored data obtained with mNG reporter
335 viruses, showing that the identified genes were *bona fide* proviral factors and not genes

336 the KO of which would only protect cells from virus-induced cell death. Encouragingly,
337 based on a recent scRNA-seq study [40], the best-validated candidate genes, i.e. *AP1G1*,
338 *AB1B1*, *AAGAB*, *KMT2C*, *EP300* and *ATP8B1*, were all well expressed in SARS-CoV-2
339 target cells from the respiratory epithelia (**Fig. S3b**). Moreover, using RT-qPCR, we
340 observed that these genes were all expressed at slightly higher levels in primary human
341 airway epithelial cells (HAE) compared to Calu-3 cells (**Fig. S3c**).
342
343 We then investigated the effect of these genes on other respiratory viruses. Noteworthy,
344 knockout had no substantial impact on the replication of a respiratory virus from another
345 family, the orthomyxovirus influenza A virus (IAV) strain A/Victoria/3/75 (H3N2) (**Fig. 3b**).
346 In contrast, HCoV-NL63 replication was impacted by *AP1G1*, *AP1B1* and *EP300* KO, but
347 not by *KMT2C* or *ATP8B1* KO (**Fig. 3c**). Interestingly, seasonal HCoV-229E and highly
348 pathogenic MERS-CoV, which do not use ACE2 for viral entry but ANPEP and DPP4,
349 respectively, were also both strongly affected by *AP1G1*, and, to some extent, by *AP1B1*
350 and *AAGAB* KO (**Fig. 3d-f**), showing a pan-coronavirus role of these genes.
351
352

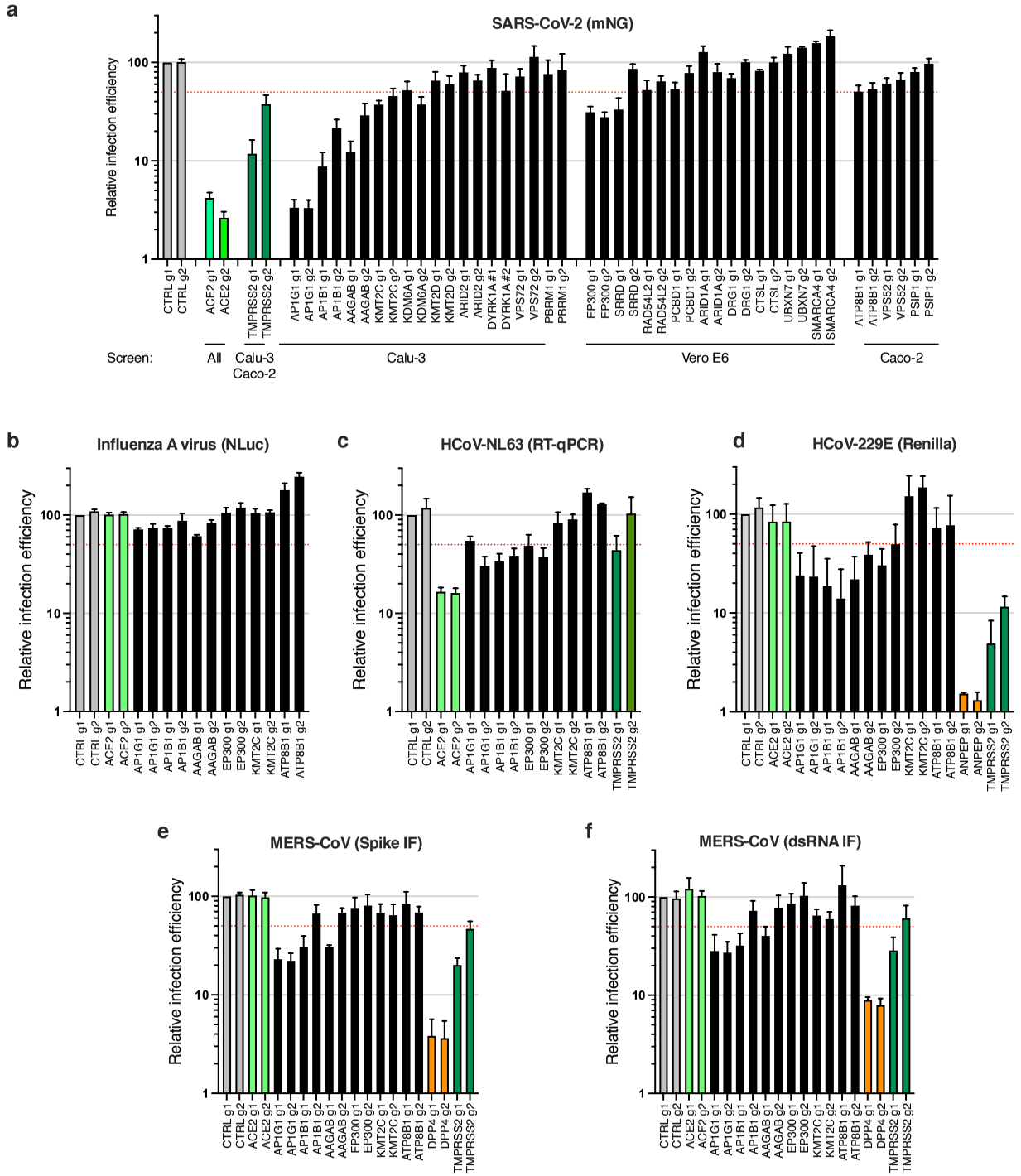

Fig. 3. Impact of the identified proviral genes on coronaviruses SARS-CoV-2, HCoV-229E, HCoV-NL63, MERS-CoV and on orthomyxovirus influenza A.
Calu-3-Cas9 cells were stably transduced to express 2 different sgRNAs (g1, g2) per indicated gene and selected for 10-15 days.

a. Cells were infected with SARS-CoV-2 bearing the mNeonGreen (mNG) reporter and the infection efficiency was scored 48h later by flow cytometry. The cell line/screen in which the candidates were identified is indicated below the graph.
b. Cells were infected with influenza A virus bearing the Nanoluciferase (NLuc) reporter and 10h later relative infection efficiency was measured by monitoring Nluc activity.
c. Cells were infected with HCoV-NL63 and 5 days later, relative infection efficiency was determined using RT-qPCR.
d. Cells were infected with HCoV-229E-Renilla and 48-72h later, relative infection efficiency was measured by monitoring Renilla activity.
e-f. Cells were infected with MERS-CoV and 16h later, the percentage of infected cells was determined using anti-Spike (**e**) or anti-dsRNA (**f**) immunofluorescence (IF) staining followed by microscopy analysis (10 fields per condition).
The mean and SEM of 4 to 7 independent experiments (**a**; with the notable exception of the genes with no validated impact in Calu-3 cells, i.e. *DYRK1A*, *VPS72*, *PBRM1*, *DRG1*, *UBXN7*, *CRSL1*, *SMARCA4*, n=2), 3 (**b**, **d**, **e**, **f**), or 2 (**c**) independent experiments. The red dashed line represents 50% inhibition.

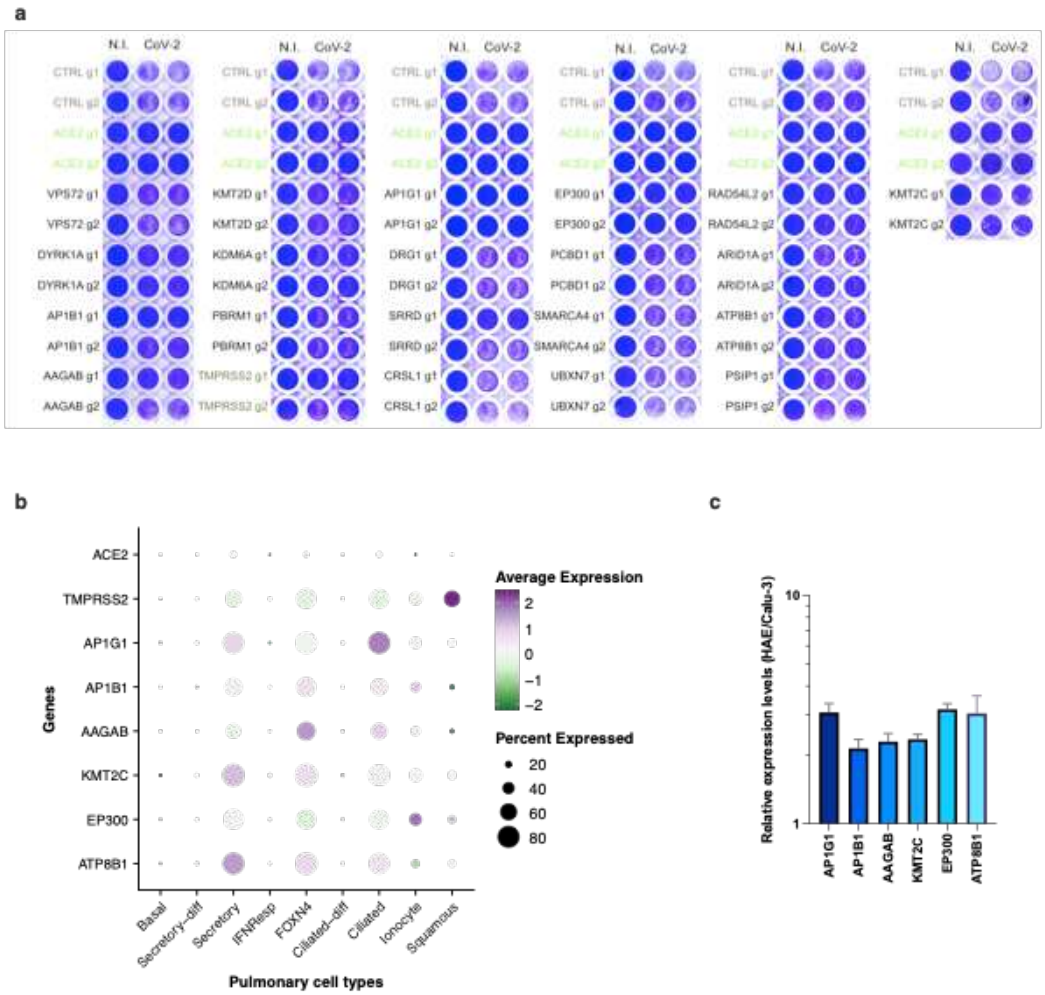

Fig. S3.
a. SARS-CoV-2 induced cytopathic effects in candidate KO cell lines.
Calu-3-Cas9 cells were stably transduced to express 2 different sgRNAs (g1, g2) per indicated gene and selected for 10-15 days. Cells were infected by SARS-CoV-2 at MOI 0.005 and ~5 days later stained with crystal violet. Representative images are shown.

381 **b. Dot plot depicting the expression levels of the best validated genes in the different cell types**
382 **from the respiratory epithelium**, from Chua et al. data set [40]. Expression levels in COVID-19 versus
383 healthy patients are color coded; the percentage of cells expressing the respective gene is size coded, as
384 indicated.
385 **c. Relative expression levels of the identified dependency factors in primary human airway epithelial**
386 **(HAE) cells compared to Calu-3 cells**. RNA samples from 3 independent experiments (and 3 independent
387 donors for HAE cells), described in [30], were analyzed by RT-qPCR using the indicated taqmans.
388

389 Next, we aimed to determine the life cycle step affected by the candidate KOs and we
390 examined the impact of the best validated candidate KO (i.e. with an effect >50%
391 decrease in mNG reporter expression, **Fig. 4a**) on ACE2 global expression levels (**Fig.**
392 **4b**). Immunoblot analysis revealed similar or higher expression levels of ACE2 in the
393 different KO cell lines in comparison to controls, with the exception of *ACE2* and *EP300*
394 KO cells, which had decreased levels of ACE2. We then took advantage of recombinant
395 Spike Receptor Binding Domain (RBD) fused to a mouse Fc fragment, in order to stain
396 ACE2 at the cell surface (**Fig. 4c**). Using this system, we did not observe a substantial
397 decrease in ACE2 at the plasma membrane, apart from *ACE2* and *EP300* KO cell lines,
398 as expected.
399

400 In order to assess the internalization efficiency of viral particles, we then incubated the
401 KO cell lines with SARS-CoV-2 at an MOI of 5 for 2h at 37°C, and treated the cells with
402 Subtilisin A in order to eliminate the cell surface-bound viruses, followed by RNA
403 extraction and RdRp RT-qPCR to measure the relative amounts of internalized viruses
404 (**Fig. 4d**). This approach showed that *AP1G1*, *AP1B1*, *AAGAB* and *EP300* impacted
405 SARS-CoV-2 internalization to at least some extent, but not *ATP8B1*. We then used
406 vesicular stomatitis virus (VSV) particles pseudotyped with SARS-CoV-2 Spike, bearing
407 a C-terminal deletion of 19 aminoacids (hereafter named Spike del19) as a surrogate for
408 viral entry [41,42], in comparison to VSV-G pseudotypes (**Fig. 4e**). Of note, both *ACE2* and
409 *TMPRSS2* knockout specifically impacted Spike del19-VSV infection, confirming that the
410 pseudotypes mimicked wild-type SARS-CoV-2 entry in Calu-3 cells. We observed that
411 Spike del19-dependent entry was affected in most cell lines in comparison to VSV-G-
412 mediated entry, with, again, the notable exception of *ATP8B1* KO cells, implying a later
413 role for this gene. Analysis of SARS-CoV-2 RNA replication by RdRp RT-qPCR (**Fig. 4f**)

414 and viral production in the cell supernatants by plaque assays (**Fig. 4g**) perfectly mirrored
415 the data obtained using the mNG reporter virus, apart from *ATP8B1* KO cells. Indeed, in
416 the latter, there was only around 50% decrease in viral RNA replication or mNG reporter
417 expression, but more than one order of magnitude decrease in viral production,
418 suggesting a late block during viral replication (**Fig. 4f-g**). Importantly, highly similar
419 results were obtained with MERS-CoV for *AP1G1* and *AP1B1*, which had an impact
420 comparable to *DPP4* receptor KO on viral production (**Fig. 4h**). Moreover, as observed
421 for SARS-CoV-2, *ATP8B1* KO also strongly impacted infectious MERS-CoV particle
422 production/release, whereas it did not impact infection as measured by Spike or dsRNA
423 intracellular staining (**Fig. 4h** and **3e-f**), arguing for a common and late role of this gene
424 in the coronavirus replicative cycle.

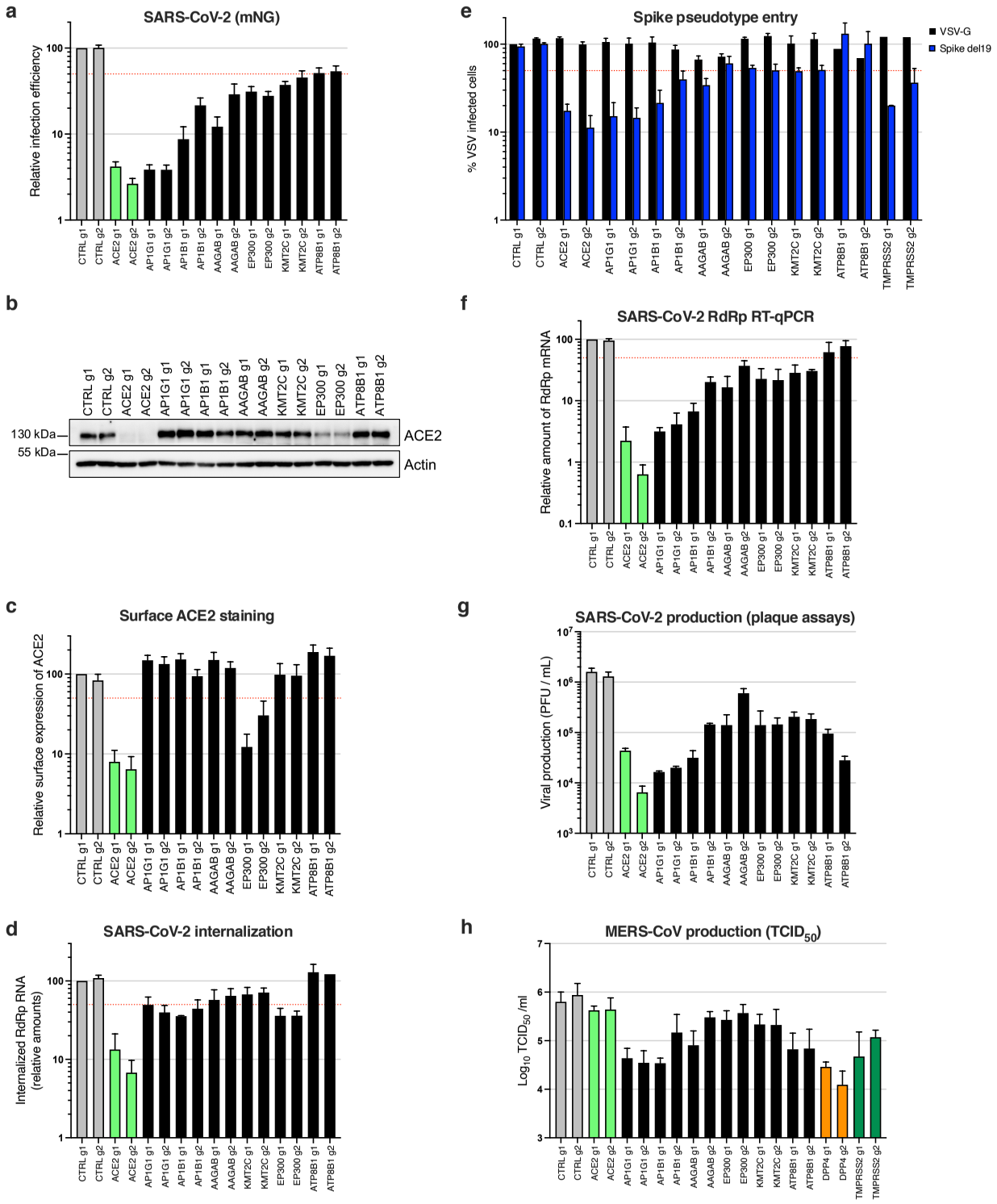

Fig. 4. Characterization of the impact of identified SARS-CoV-2 dependency factors. Calu-3-Cas9 cells were stably transduced to express 2 different sgRNAs (g1, g2) per indicated gene and selected for 10-15 days.

a. Cells were infected with SARS-CoV-2 bearing the mNG reporter and the infection efficiency was scored 48h later by flow cytometry.

b. The expression levels of ACE2 were analyzed by immunoblot, Actin served as a loading control.

c. Relative surface ACE2 expression was measured using a Spike-RBD-Fc fusion and a fluorescent secondary antibody followed by flow cytometry analysis.
d. Cells were incubated with SARS-CoV-2 at MOI 5 for 2h at 37°C and then treated with Subtilisin A followed by RNA extraction and RdRp RT-qPCR analysis as a measure of viral internalization.
e. Cells were infected with Spike del19 and VSV-G pseudotyped, GFP expressing VSV and infection efficiency was analyzed 24h later by flow cytometry.
f. Cells were infected with SARS-CoV-2 at MOI 0.05 and, 24h later, lysed for RNA extraction and RdRp RT-qPCR analysis.
g. Aliquots of the supernatants from F were harvested and plaque assays were performed to evaluate the production of infectious viruses in the different conditions.
h. Cells were infected with MERS-CoV and 16h later, infectious particle production in the supernatant was measured by $TCID_{50}$.
The mean and SEM of at least 5 (**a**), 3 (**c**, **d**, **e**, **f**, **h**) independent experiments or representative experiments (**b** and **g**) are shown. The red dashed line represents 50% inhibition (**a**, **c-f**).

CRISPR activation screen reveals new anti-SARS-CoV-2 genes, including *Mucins*, *CD44* and *IL6R*

Next, 21 genes among the top-ranking hits conferring resistance to SARS-CoV-2 replication from the CRISPRa screen were selected for individual validation, using two different sgRNAs in Calu-3-dCas9-VP64 cells. In parallel, non-targeting sgRNAs and sgRNAs targeting *ACE2* and *IFNL2* promoters were used as controls. 10-15 days post-transduction, the sgRNA-expressing cell lines were challenged with SARS-CoV-2 bearing the mNG reporter, as previously, and the percentage of infected cells was scored by flow cytometry (**Fig. 5a**). As expected [30,35,43], the induction of *IFNL2* and *LY6E* expression potently decreased SARS-CoV-2 replication. We observed that the increased expression of the vast majority of the selected hits induced at least a 50% decrease in infection efficiency with at least 1 of the 2 sgRNAs. Some genes had a particularly potent impact on SARS-CoV-2 and decreased the replication levels by 80-90% or more, including the Mucin genes *MUC1*, *MUC21*, *MUC4*, as well as *CD44*, *PLAGL1*, *IL6R*, *TEAD3* and *LYN* (**Fig. 5a**). *CD44* codes for a cell surface transmembrane glycoprotein playing multiple roles in adhesion, cell proliferation and survival, signaling, migration, or lymphocyte activation [44,45]. *PLAGL1* codes for a zinc finger transcription factor that promotes cell cycle arrest and apoptosis through multiple pathways [46]. *IL6R* (also known as gp80 or CD126) codes for a membrane-bound as well as a soluble receptor for IL6; IL6R is bound to gp130 (or CD130), which mediates signal transduction. Upon binding of IL6 to IL6R, the

468 homodimerization of gp130 is induced and a hexameric complex constituted of
469 IL6/IL6R/gp130 is formed, which induce a signaling cascade through the JAK/STAT and
470 SHP-2/ERK MAPK pathways regulating a variety of biological activities, including host
471 defense [47]. *TEAD3* codes for a member of transcriptional enhancer factor (TEF) family of
472 transcription factors and plays roles in development, cell differentiation as well as
473 proliferation [48,49]. *LYN* codes for a membrane-anchored src tyrosine kinase, localized on
474 the cytoplasmic side of the plasma membrane and is an important regulator of signal
475 transduction [50]. Noteworthy, LYN was shown to regulate inflammatory responses to
476 bacterial infection [51] and to be important for flavivirus egress [52]. Additionally, an scRNA
477 seq study had shown that most of the antiviral genes identified here were expressed in a
478 substantial percentage of epithelial cells from the respiratory epithelium, including ciliated
479 cells and secretory cells, the main targets of SARS-CoV-2 (**Fig. S4a**, based on [40]). We
480 confirmed that primary human airway epithelial cells (HAE) expressed *MUC1*, *MUC4*,
481 *MUC21*, *CD44*, *IL6R*, *TEAD3* and *LYN* (**Fig. S4b**). Interestingly, all these genes were
482 expressed to higher levels in HAE than Calu-3 cells, with the exception of *CD44*, which
483 was less expressed. Moreover, *MUC21* was upregulated upon SARS-CoV-2 replication
484 in HAE and Calu-3 cells, as well as *MUC4* in the latter (**Fig. S4c-d**).
485
486 Looking at the antiviral breadth of the validated genes, we observed that the induction of
487 most of them had no impact on IAV infection (**Fig. 5b**), with the exception of *MUC4* and
488 *MUC1,* which decreased the infection efficiency by ~60-70%, as seen previously [37], and
489 *IL6R,* with one of the 2 sgRNAs leading to 75% decrease in infection efficiency.
490 Interestingly, similarly to SARS-CoV-2, HCoV-229E appeared highly sensitive to the
491 increased expression of *MUC*s, *IL6R*, *LY6E*, *CD44*, but was less affected or not affected
492 at all by the other genes, such as *PLAGL1* (**Fig. 5c**). MERS-CoV infection was impacted
493 by the 3 *Mucin*s of interest and to some extent by *PLAGL1*, *CD44*, *IL6R*, *LY6E* and
494 *ATAD3B*, but not by the other candidates (**Fig. 5d**).
495
496

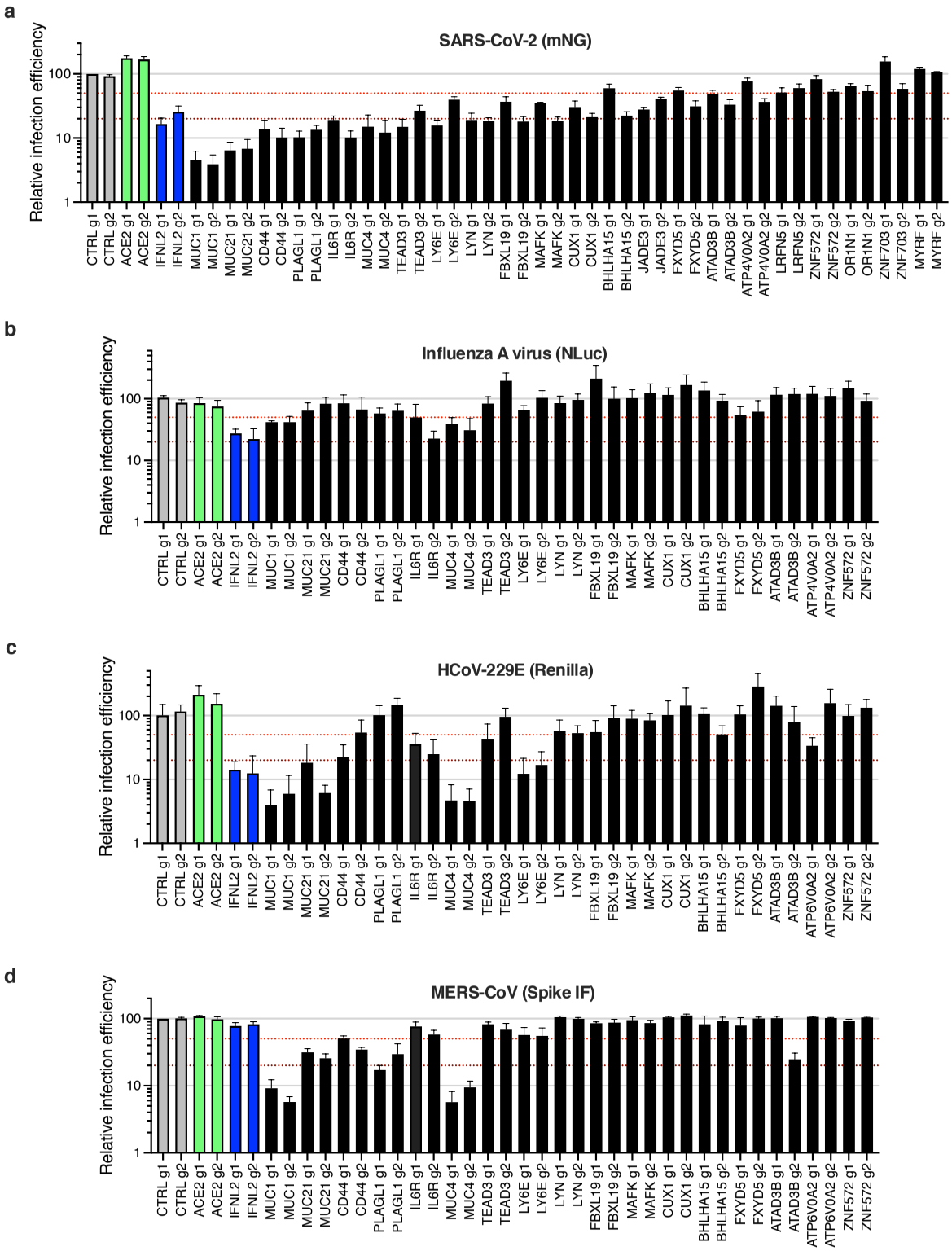

Fig. 5. Impact of the identified antiviral genes on coronaviruses SARS-CoV-2, HCoV-229E, and MERS-CoV, and on orthomyxovirus influenza A.
Calu-3-dCas9-VP64 cells were stably transduced to express 2 different sgRNAs (g1, g2) per indicated gene promoter or negative controls (CTRL) and selected for at least 10-15 days.

a. Cells were infected with SARS-CoV-2 bearing the mNG reporter and the infection efficiency was scored 48h later by flow cytometry.
b. Cells were infected with influenza A virus bearing the Nanoluciferase (NLuc) reporter and 10h later relative infection efficiency was measured by monitoring Nluc activity.
c. Cells were infected with HCoV-229E-Renilla and 48-72h later, relative infection efficiency was measured by monitoring Renilla activity.
d. Cells were infected with MERS-CoV and 16h later, the percentage of infected cells was determined using anti-Spike IF staining followed by microscopy analysis (10 fields per condition).
The mean and SEM of at least 4 (**a**) or 3 (**b**, **c**, **d**) independent experiments are shown. The red and dark red dashed lines indicate 50% and 80% inhibition, respectively.

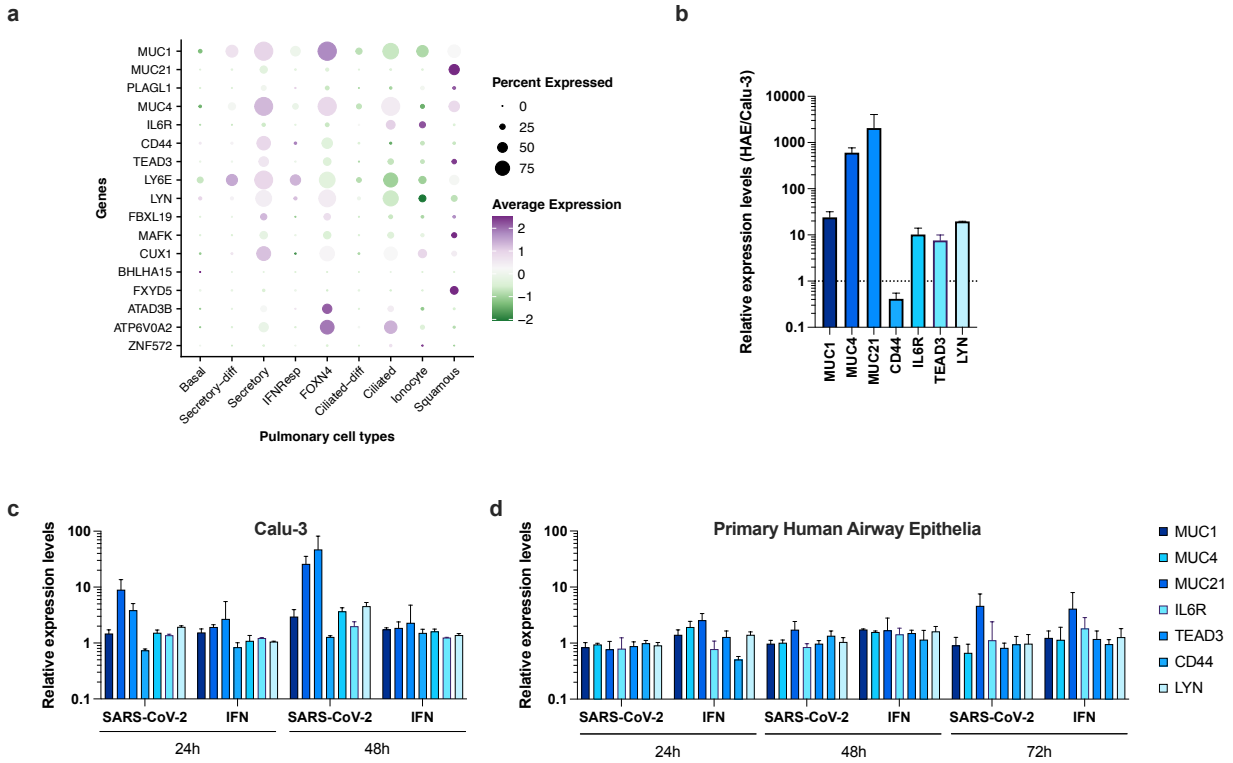

Fig. S4.
a. Dot plot depicting the expression levels of the best validated antiviral genes in the different cell types from the respiratory epithelium, from Chua et al. data set [40]. Expression levels in COVID-19 versus healthy patients are color coded; the percentage of cells expressing the respective gene is size coded, as indicated.
b. Relative expression levels of a selection of the antiviral factors in primary human airway epithelial cells (HAE) compared to Calu-3 cells. RNA samples from 3 independent experiments, described in [30], were analyzed by RT-qPCR using the indicated taqmans.
c-d. Impact of SARS-CoV-2 infection and interferon treatment on antiviral factor expression in HAE (**c**) **and Calu-3 cells** (**d**), as indicated, in samples from 3 independent experiments from [30].

Next, we tested the impact on SARS-CoV-2 of some of the best candidates in naturally permissive Caco-2 cells and in A549 cells engineered to ectopically express ACE2 (**Fig.**

528 **S5**). We observed that *MUC4*, *MUC1, MUC21* induction potently decreased SARS-CoV-
529 2 infection in these two other cell lines. Moreover, *PLAGL1* also had a strong impact in
530 A549-ACE2 cells but not in Caco-2 cells, and the opposite was true for *LYN*. This might
531 suggest a potential cell type specificity for the former (e.g. lung origin) and possibly a
532 dependence on ACE2/TMPRSS2 endogenous expression for the latter. *CD44* and *LY6E*
533 also had an inhibitory effect to some extent in both cell lines. Taken together, this globally
534 showed that the inhibitory effect of the validated candidates is not restricted to Calu-3
535 cells and can be observed in other cell types.
536

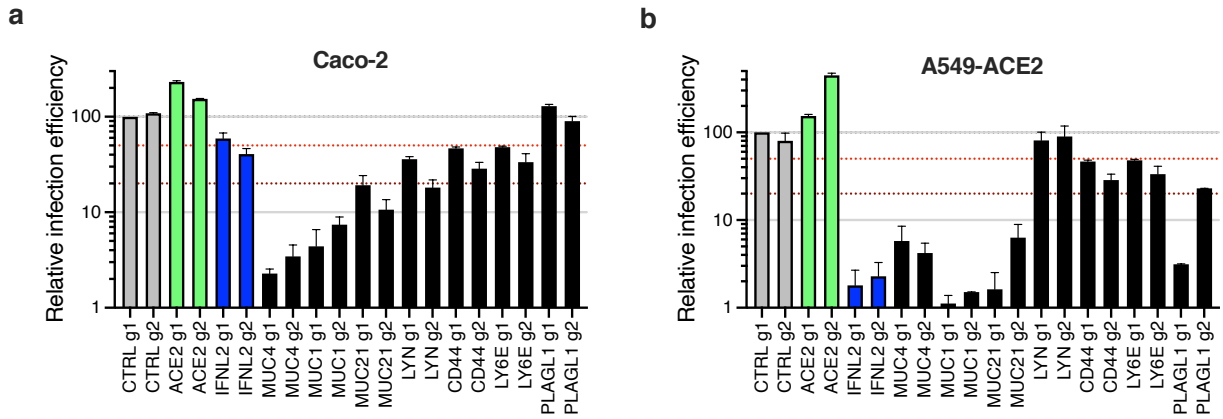

537

538 **Fig. S5. Impact of the identified antiviral genes on SARS-CoV-2 in Caco-2 and A549-ACE2 cells.**
539 Caco-2-dCas9-VP64 (**a**) and A549-ACE2-dCas9-VP64 (**b**) cells were stably transduced to express 2
540 different sgRNAs (g1, g2) per indicated gene promoter, or negative controls (CTRL) and selected for at
541 least 10-15 days prior to SARS-CoV-2 mNG infection. The percentage of infected cells was scored 48h
542 later by flow cytometry. Relative infection efficiencies (mean and SEM) are shown for 2 independent
543 experiments. The red and dark red dashed lines represent 50% and 80% inhibition, respectively.
544

545 We then explored the life cycle step affected by antiviral gene expression. The SARS-
546 CoV-2 internalization assay, performed as previously, showed that most of the validated
547 genes, including those showing the strongest inhibitory phenotypes (namely *MUC1*,
548 *MUC21*, *CD44*, *PLAGL1*, *IL6R*, *MUC4*, and *LYN*) impacted viral internalization (**Fig. 6a**).
549 The measure of viral entry using Spike del19- or G-pseudotyped VSV particles globally
550 mirrored the internalization data, and showed that G-dependent entry was as sensitive as
551 Spike del19-dependent entry to the induced expression of *Mucins*, *IL6R* or *LYN* (**Fig. 6b**).
552 However, we observed that whereas *CD44* and *PLAGL1* had an impact on SARS-CoV-2
553 entry as measured by our internalization assay (as well as a number of other genes such

554 as *TEAD3*, but with milder effects), there was no effect of these genes on Spike del19-
555 VSV pseudotypes, perhaps highlighting subtle differences in the mechanism of entry by
556 the latter compared to wild-type SARS-CoV-2. Moreover, *LY6E* induction had no
557 measurable impact on viral entry, either using the internalization assay or the VSV
558 pseudotype assay, contrary to what was reported before [35]. Differences in the
559 experimental systems used could explain the differences observed here and would
560 require further investigation. Finally, the impact of the best candidates on SARS-CoV-2
561 and MERS-CoV replication, measured by RdRp RT-qPCR (**Fig. 6c**) and plaque assays
562 (**Fig. 6d**) for SARS-CoV-2, or $TCID_{50}$ for MERS-CoV (**Fig. 6e**), recapitulated what was
563 observed with SARS-CoV-2 mNG reporter (**Fig. 5a**) and MERS-CoV Spike intracellular
564 staining (**Fig. 5d**).
565
566 Noteworthy, the 3 Mucins of interest had the strongest impact on both SARS-CoV-2 and
567 MERS-CoV production (~2 log and ~1 log decrease, respectively, as compared to the
568 controls). The activation of *IL6R*, *CD44*, *PLAGL1*, and *LYN* also had a substantial impact
569 on SARS-CoV-2 replication (~1 log decrease or more, for at least 1 out of the 2 sgRNAs)
570 but had a globally milder impact on MERS-CoV replication, with *LYN* having no impact at
571 all (**Fig. 6d-e**). Whereas Mucins are well-known to act as antimicrobial barriers [53,54], the
572 role of the other potent antiviral genes, such as *IL6R*, *CD44* or *PLAGL1*, in limiting SARS-
573 CoV-2 entry remains to be elucidated.

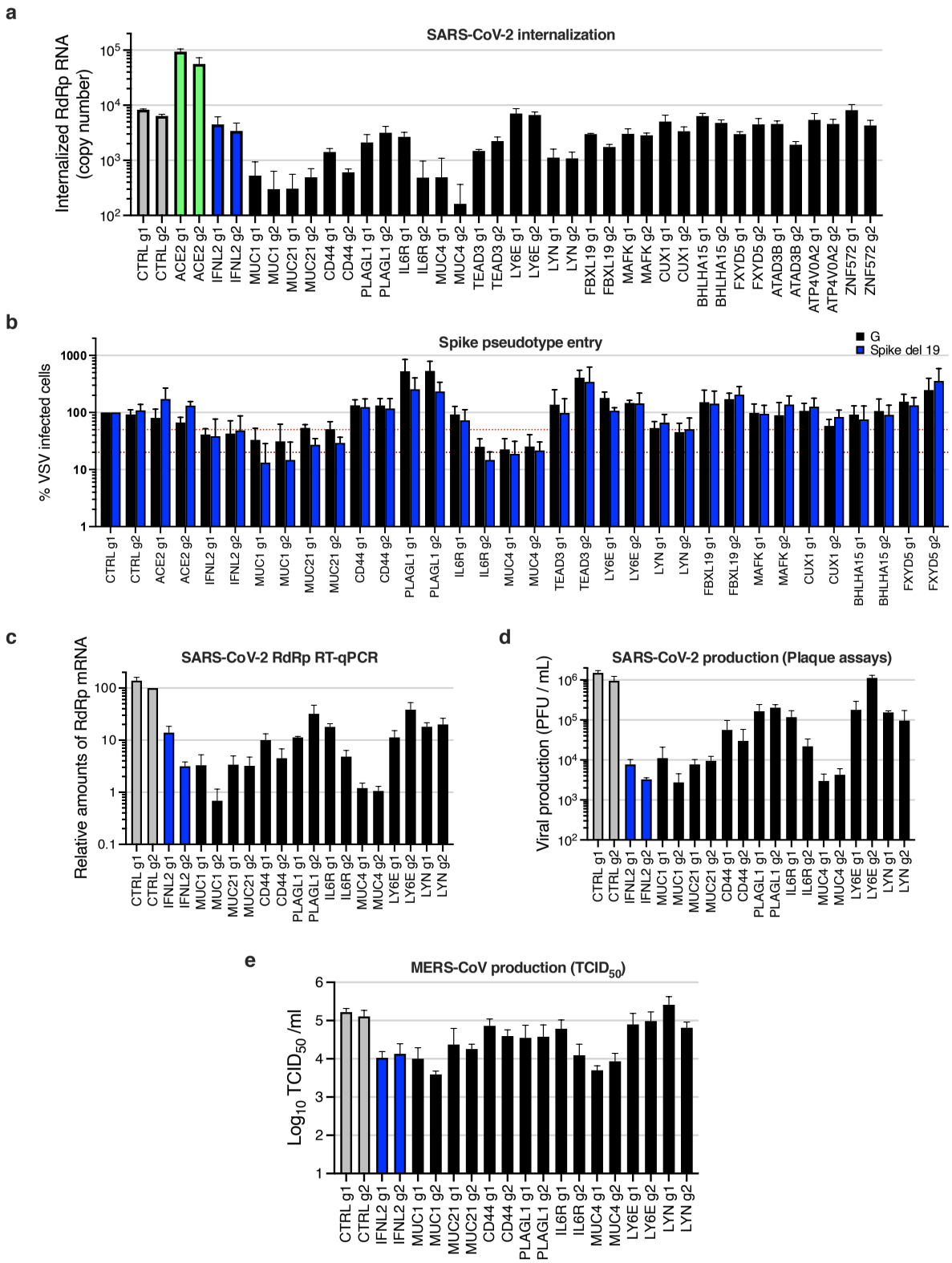

Fig. 6. Characterization of the impact of identified SARS-CoV-2 dependency factors.
Calu-3-dCas9-VP64 cells were stably transduced to express 2 different sgRNAs (g1, g2) per indicated gene promoter and selected for 10-15 days.

578 **a**. Cells were incubated with SARS-CoV-2 at MOI 5 for 2h and then treated with Subtilisin A followed by
579 RNA extraction and RdRp RT-qPCR analysis.
580 **b.** Cells were infected with Spike del19 and VSV-G pseudotyped, Firefly-expressing VSV and infection
581 efficiency was analyzed 24h later by monitoring Firefly activity. The red and dark red dashed lines represent
582 50% and 80% inhibition, respectively.
583 **c**. Cells were infected with SARS-CoV-2 at MOI 0.05 and, 24h later, lysed for RNA extraction and RdRp
584 RT-qPCR analysis.
585 **d**. Aliquots of the supernatants from C were harvested and plaque assays were performed to evaluate the
586 production of infectious viruses in the different conditions. A representative experiment is shown.
587 **e**. Cells were infected with MERS-CoV and 16h later, infectious particle production in the supernatant was
588 measured by $TCID_{50}$.
589 The mean and SEM of 3 (**a**, **c**), 4 (**b**), 2 (**d**, **e**) independent experiments are shown.
590

591

592 Individual validations via CRISPR activation reveal additional pro-SARS-CoV-2 genes, 593 including *TP73* and *NFE2*

594 In addition to the dependency factors identified by the KO screens, we selected several
595 of the top-ranking hits conferring sensitization to SARS-CoV-2 replication in the CRISPRa
596 screen. Solute carriers SLC6A14 and SLC6A19, transcription factors Tumor Protein P73
597 (TP73), Hepatocyte nuclear factor-1β (HNF1B) and Nuclear Factor, Erythroid 2 (NFE2)
598 were chosen for individual validations, using two different sgRNAs in Calu-3-dCas9-VP64
599 cells in parallel to controls, as previously. At least 12-15 days post-transduction, the
600 sgRNA-expressing cell lines were challenged with SARS-CoV-2 bearing a NLuc reporter
601 [55] and the relative infection efficiency was analyzed by monitoring NLuc activity (**Fig. 7a**).
602 Among the tested candidates, *TP73*, *HNF1B*, and *NFE2* had the strongest positive impact
603 on SARS-CoV-2 replication (~3-4-fold increase), which was comparable to what was
604 observed with *ACE2* overexpression. *SLC6A19* induction had a slight positive effect on
605 SARS-CoV-2 infection (~1.5-2-fold). Surprisingly, the induced-expression of *SLC6A14*,
606 which was the top-ranking sensitizing hit after ACE2, had an inhibitory effect on SARS-
607 CoV-2 infection rather than a positive effect, when measuring NLuc reporter activity.
608 However, SARS-CoV-2-induced CPEs were increased in *SLC6A14*-induced cells
609 compared to the control, suggesting a late impact of this gene on viral replication and/or
610 an increase in cell death (**Fig. 7b**). Interestingly, none of the identified proviral factors had
611 a positive impact on influenza A virus infection, with the notable exception of *HNF1B*,
612 which had a slight positive impact (**Fig. 7c**). In contrast, all the identified proviral genes

613 had a positive impact on HCoV-NL63 infection (**Fig. 7d**). We then studied the impact of
614 the candidates on HCoV-229E, using in parallel 2 sgRNAs targeting *ANPEP* as positive
615 controls (**Fig. 7e**). Calu-3 cells are known to express low levels of ANPEP [56], and, as
616 expected, *ANPEP* receptor induction greatly increased HCoV-229E infection in Calu-3
617 cells. Among the genes having a positive impact on SARS-CoV-2 and HCoV-NL63, only
618 *TP73* induction had a positive effect on HCoV-229E infection (**Fig. 7e**).

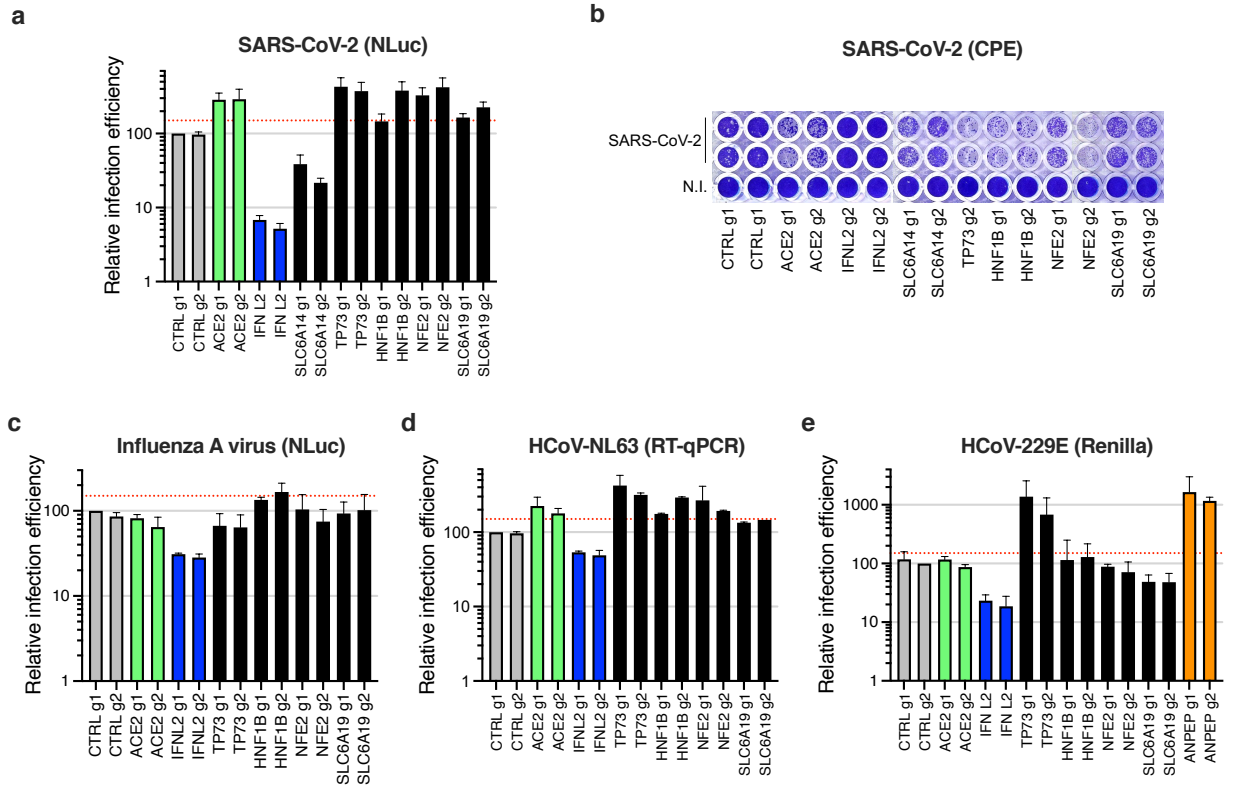

619

620 **Fig. 7. Impact of the proviral genes identified by CRISPRa on coronaviruses SARS-CoV-2, HCoV-**
621 **229E, HCoV-NL63 and on orthomyxovirus influenza A.**
622 Calu-3-dCas9-VP64 cells were stably transduced to express 2 different sgRNAs (g1, g2) per indicated gene
623 promoter and selected for 10-15 days.
624 **a.** Cells were non infected (N.I.) or incubated with SARS-CoV-2 bearing NLuc reporter and the infection
625 efficiency was scored 30 h later by monitoring NLuc activity.
626 **b.** Cells were infected by SARS-CoV-2 at MOI 0.05 and ~5 days later stained with crystal violet.
627 Representative images from 2 independent experiments are shown.
628 **c.** Cells were infected with influenza A virus bearing NLuc reporter and 10h later, relative infection efficiency
629 was measured by monitoring NLuc activity.
630 **d.** Cells were infected with HCoV-NL63 and 5 days later, infection efficiency was determined using RT-
631 qPCR.
632 **e.** Cells were infected with HCoV-229E-Renilla and 72h later, relative infection efficiency was measured by
633 monitoring Renilla activity.
634 The mean and SEM of 4 (**a**), 3 (**c**, **e**) or 2 (**d**) independent experiments or representative images (**b**) are
635 shown. The red dashed line indicates 1,5-fold increase in infection efficiency.

636 In order to decipher the step(s) affected by the induction of the identified proviral genes,
637 we used SARS-CoV-2 internalization and VSV pseudotype assays (**Fig. 8a-b**), as
638 previously. Using these 2 assays, we observed that induction of both *HNF1B* and *NFE2*
639 improved viral entry, but not *TP73* or *SLC6A19*, which was surprising for the latter as it is
640 a known partner of ACE2 [33]. In line with this, we observed that, despite differences in
641 ACE2 levels in the 2 negative control cell lines, induction of *HNF1B* and *NFE2* seemed
642 to increase ACE2 expression, contrary to that of *TP73* or *SLC6A19* (**Fig. S6a**). *TP73* and
643 *SLC6A19* induction, however, increased SARS-CoV-2 RdRp RNA amounts in infected
644 cells as well as infectious particle production, arguing for a post-entry impact on
645 replication (**Fig. 8c-d**). Interestingly, the pan-coronavirus cofactor *TP73* (**Fig. 7**) was
646 particularly well expressed in ciliated cells from the respiratory epithelium, and SARS-
647 CoV-2 infection in patients positively modulated its expression (**Fig. S6b**; [40]). TP73 is
648 known to be a pro-apoptotic transcription factor, inducing apoptosis upon DNA damage
649 and regulating DNA damage repair [57–59]. However, here we show that TP73 does not just
650 play a role in enhancing SARS-CoV-2-induced cell death, as its induction increases viral
651 replication and production. TP73 could be acting indirectly, through the induced
652 expression of SARS-CoV-2 cofactors. Interestingly, although expressed in a lower
653 percentage of cells as compared to *TP73*, *HNF1B* expression was also upregulated in
654 ciliated cells from COVID-19 patients compared to healthy controls [40] (**Fig. S6b**). HNF1B
655 is a homeodomain containing transcription factor that regulates tissue-specific gene
656 expression positively or negatively, and HNF1B has been shown to modulate lipid
657 metabolism [60], which might be related to its positive role on SARS-CoV-2 entry, in addition
658 to the observed increase of ACE2 expression. NFE2 is a transcription factor involved in
659 erythroid and megakaryocytic maturation and differentiation and, together with MAFK
660 (which was identified as an antiviral gene by our CRISPRa screen, **Fig. 2C** and **5a**), forms
661 a complex, which regulates various pathways [61]. Interestingly, genes regulated by MAFK
662 and NFE2 were both identified as differentially expressed upon SARS-CoV-1 replication
663 [62].

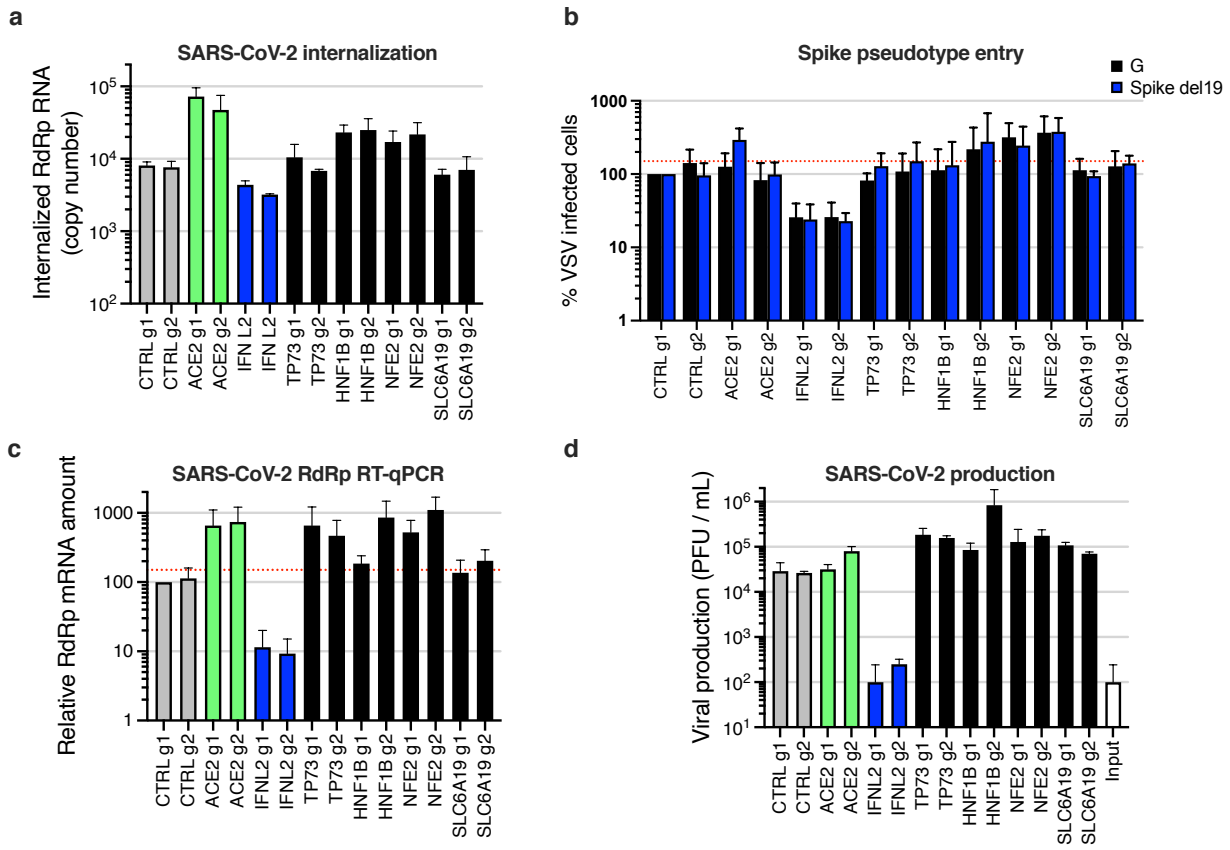

Fig. 8. SARS-CoV-2 life cycle steps affected by the proviral gene induction.
Calu-3-dCas9-VP64 cells were transduced to express 2 different sgRNAs (g1, g2) per indicated gene promoter and selected for 10-15 days.
a. Cells were incubated with SARS-CoV-2 at MOI 5 for 2h at 37°C and then treated with Subtilisin A followed by RNA extraction and RdRp RT-qPCR analysis as a measure of viral internalization.
b. Cells were infected with Spike del19 and VSV-G pseudotyped, Firefly-expressing VSV and infection efficiency was analyzed 24h later by monitoring Firefly activity.
c. Cells were infected with SARS-CoV-2 at MOI 0.05 and, 24h later, lysed for RNA extraction and RdRp RT-qPCR analysis.
d. Aliquots of the supernatants from C were harvested and plaque assays were performed to evaluate the production of infectious viruses in the different conditions.
The mean and SEM of 3 (**a**, **b**, **c**) or 2 (**d**) independent experiments are shown. The red dashed line indicates 1,5-fold increase in infection efficiency.

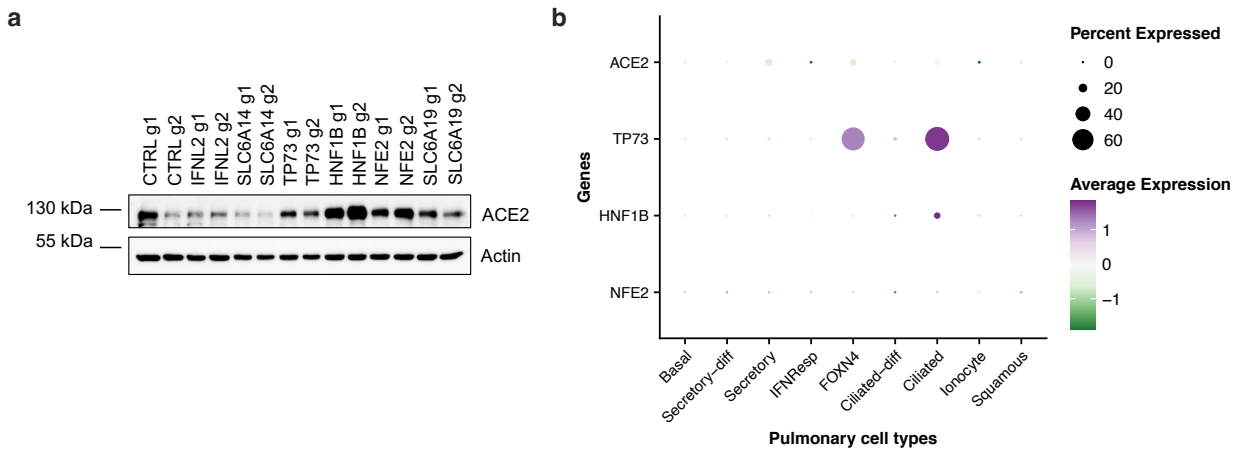

Fig. S6.
a. ACE2 expression in CRISPRa cell lines.
Calu-3-Cas9 cells were stably transduced to express 2 different sgRNAs (g1, g2) per indicated gene and selected for 10-15 days (parallel samples from **Fig. 7- 8**). The cells were lysed and expression levels of ACE2 were analyzed, Actin served as a loading control. A representative immunoblot is shown.
b. Dot plot depicting the expression levels of the best validated proviral genes in the different cell types from the respiratory epithelium, from Chua et al. data set [40]. Expression levels in COVID-19 versus healthy patients are color coded; the percentage of cells expressing the respective gene is size coded, as indicated.

Discussion

Despite intense research efforts, much remains to be discovered about the host factors regulating replication of SARS-CoV-2 and other coronaviruses. Recently, a number of whole-genome CRISPR KO screens successfully identified coronavirus host-dependency factors pandemics [23–28]. However, most of these screens relied on ACE2 ectopic expression and were performed in cells which do not express TMPRSS2, an important cofactor for entry [8] (with one notable exception [26], which relied on TMPRSS2 ectopic expression). A meta-analysis of these screens revealed a high-level of cell type specificity in the hits identified, indicating a need to pursue such efforts in other model cell lines, in order to better define the landscape of SARS-CoV-2 cofactors. In the present study, we performed bidirectional, genome-wide screens in physiologically relevant lung Calu-3 cells, as well as KO screens in intestinal Caco-2 cells. We identified new host-dependency factors, which are not only essential for SARS-CoV-2 replication but also for

705 other coronaviruses, namely MERS-CoV, HCoV-229E and HCoV-NL63. Furthermore,
706 our study unraveled new antiviral genes, some of them with potent and/or broad anti-
707 coronavirus activity.
708
709 Simultaneously to our screens, similar bidirectional, genome-wide screens were
710 performed in Calu-3 cells by P. Hsu and colleagues [63]. Comparisons between our data
711 sets and theirs showed a very good overlap in the hits identified, both in the KO and
712 activation screens (**Fig. S7**), with shared hits including host-dependency factors Adaptins
713 AP1G1 and AP1B1 as well as Mucins as antiviral proteins. Interestingly, ATP8B1, which
714 was identified in our Caco-2 KO screen, scored within the 25 best hits in Hsu and
715 colleagues' Calu-3 KO screen, showing the complementarity of our data. This comparison
716 emphasizes the reproducibility of CRISPR screens conducted across different labs, even
717 when different libraries are used, while further highlighting that the cellular model is the
718 primary source of variability.
719

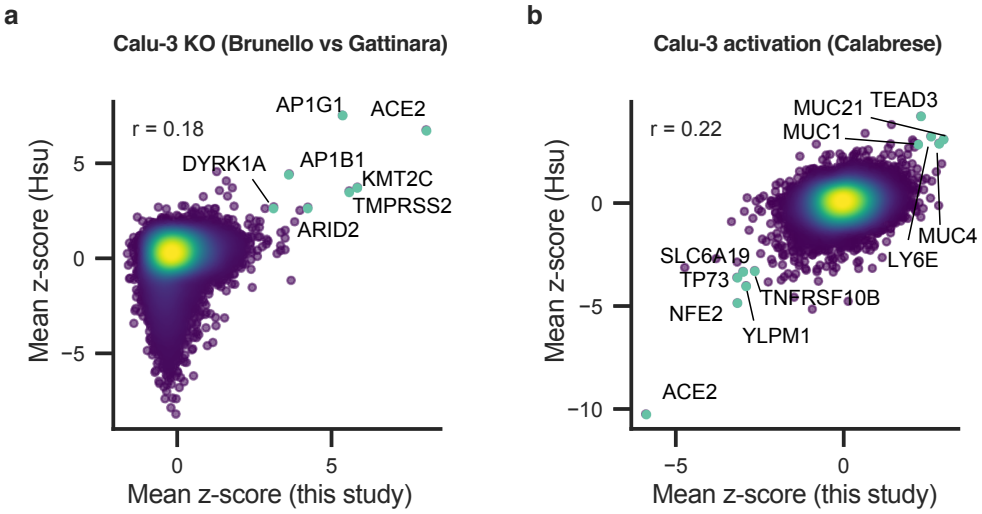

720
721 **Fig. S7.**
722 **a.** Comparison between this Calu-3 KO screen to the Calu-3 KO screen conducted by Hsu and colleagues
723 [63]. Genes that scored among the top 20 resistance hits in both screens are annotated and shown in green.
724 **b.** Comparison between this Calu-3 activation screen to the Calu-3 activation screen conducted by Hsu and
725 colleagues [63]. Genes that scored among the top 20 resistance hits and sensitization hits in both screens
726 are annotated and shown in green.
727

728 Interestingly, we observed that most of the identified genes impacted the early phases of
729 the replicative cycle. This observation was true for both the host dependency factors and
730 the antiviral inhibitors, presumably emphasizing the fact that viral entry is the most critical
731 step of the viral life cycle and probably, as such, the most easily targeted by natural
732 defenses. Among the host-dependency factors essential for viral entry, the Adaptin
733 AP1G1 and, to a lower extent, Adaptin AP1B1 and their partner AAGAB, surprisingly
734 played a crucial role. The AP-1 complex regulates polarized sorting at the trans-Golgi
735 network and/or at the recycling endosomes, and may play an indirect role in apical sorting
736 [64]. Interestingly, AAGAB has been shown to bind to and stabilize AP1G1, and in *AAGAB*
737 KO cells, AP1G1 is known to be less abundant [65], which may suggest a role of AAGAB
738 *via* the regulation of AP-1 complex here. Our data showed that the KO of *AP1G1*, *AP1B1*
739 or *AAGAB* impacted SARS-CoV-2 entry, while not affecting ACE2 expression at the cell
740 surface. In line with this observation, the KO of these factors also impacted MERS-CoV
741 and HCoV-229E, which use different receptors. However, all these coronaviruses use
742 TMPRSS2 for Spike priming in Calu-3 cells, therefore a possible explanation could be
743 that the AP-1 complex might be important for surface expression of TMPRSS2 (a
744 hypothesis that we have so far been unable to test, due to the lack of specific TMPRSS2
745 antibodies). Alternatively, the AP-1 Adaptins might be important for the proper localization
746 of other plasma membrane components, which play a role in SARS-CoV-2 attachment
747 and/or entry.
748
749 Our analysis revealed that another cofactor affecting viral entry, EP300, which is a histone
750 acetyltransferase, was most likely having an indirect effect on SARS-CoV-2 replication,
751 by regulating ACE2 expression. The fact that EP300 impacted HCoV-NL63 but not HCoV-
752 229E or MERS-CoV reinforced this hypothesis. This was also true for two proviral factors
753 identified through our CRISPRa screens, HNF1B and NFE2. In contrast, proviral factor
754 TP73 had no effect on ACE2 expression or viral entry, and actually impacted the 4
755 coronaviruses we tested here, suggesting the potential regulation of pan-coronavirus
756 factor(s) by this transcription factor.
757

758 An exception among the proviral genes that we characterized was ATP8B1, the only one
759 acting at a late stage of the viral life cycle. ATP8B1 belongs to the P4-Type subfamily of
760 ATPases (P4-ATPases) transporters, which are flippases translocating phospholipids
761 from the outer to the inner leaflet of membrane bilayers [66]. ATP8B1 has been shown to
762 be essential for proper apical membrane structure and mutations of this gene have been
763 linked to cholestasis. The fact that ATP8B1 was important for both SARS-CoV-2 and
764 MERS-CoV replication highlighted a potentially conserved role for coronaviruses and it
765 would be of high interest to understand the underlying molecular mechanisms.
766 Interestingly, ATP8B1 and its homologous ATP8B2 were recently identified as binding-
767 partners of SARS-CoV-2 ORF3 and M, respectively [67], suggesting that the virus might
768 subvert their functions. Of note, TMEM41B, an integral protein of the endoplasmic
769 reticulum known to regulate the formation of autophagosomes, lipid droplets and
770 lipoproteins, was recently shown to be both an essential coronavirus cofactor [25] and a
771 phospholipid scramblase whose deficiency impaired the normal cellular distribution of
772 cholesterol and phosphatidylserine [68]. Whether ATP8B1 could play a similar role in
773 coronavirus replication remains to be determined.
774
775 Among the best antivirals we identified through our CRISPRa screens, the well-known
776 antimicrobial defenses, membrane-associated Mucins played a broad and potent role at
777 limiting coronavirus entry. Interestingly, these Mucins were upregulated in COVID-19
778 patients [40]. Additionally, we showed that induced expression of two other membrane
779 proteins, CD44 and IL6R, could also limit SARS-CoV-2 viral entry. Both these proteins
780 are classically seen as important players during immune responses, being involved
781 mainly in adhesion/trafficking and pro-inflammatory processes, respectively. Interestingly,
782 CD44 has also been demonstrated to serve as a platform that brings other membrane
783 receptors together with actin cytoskeleton, possibly within lipid rafts [44]. One can thus
784 hypothesize that CD44 might prevent virus entry by acting on specific cellular membrane
785 domains. Regarding IL6R, it is interesting to note that Tocilizumab, a monoclonal antibody
786 against this protein, has been used in clinical trials in severe COVID-19 patients. Indeed,
787 IL-6 is one of the major cytokines responsible for the exacerbated inflammation observed

788 in severe COVID-19 patients. However, Tocilizumab did not improve the clinical outcome
789 of severe COVID-19 [69]. Although the exact molecular mechanism of action of how
790 overexpressed IL6R prevents SARS-CoV-2 entry remains to be uncovered, IL6R
791 signaling might indirectly protect lung epithelial cells from infection *via* the induction of
792 innate defenses.
793
794 In conclusion, our study unraveled a new network of SARS-CoV-2 and other coronavirus
795 regulators, in model cell lines physiologically expressing ACE2 and TMPRSS2.
796 Importantly, the main natural targets of SARS-CoV-2 in the respiratory tract do co-express
797 ACE2 and TMPRSS2 [40,70], which highlight the importance of the models used here.
798 Further characterization work on this newly identified landscape of coronavirus regulators
799 might guide future therapeutic intervention.
800
801
802

803 **Materials and Methods**
804

805 **Plasmids and constructs**

806 The lentiviral vector expressing ACE2 (pRRL.sin.cPPT.SFFV/ACE2, Addgene 145842)
807 has been described [30]. The pLX_311-Cas9 (Addgene 96924) and pXPR_BRD109, which
808 express Cas9 and dCas9-VP64, respectively, have been described [32]. LentiGuide-Puro
809 vector was a gift from Feng Zhang [71,72] (Addgene 52963) and we have described before
810 the LentiGuide-Puro-CTRL g1 and g2 [73] (Addgene 139455 and 139456). pXPR_502
811 vector for sgRNA expression for CRISPRa was also described [32] (Addgene 96923). Guide
812 RNA coding oligonucleotides were annealed and ligated into BsmBI-digested LentiGuide-
813 Puro or pXPR_502 vectors, as described (Addgene). See **Tables 2 and 3** for the sgRNA
814 coding sequences used. pcDNA3.1_spike_del19 was a gift from Raffaele De Francesco
815 (Addgene 155297).
816

817 **Cell lines**

818 Human HEK293T, Caco-2, Calu-3, A549, Huh7, and Huh7.5.1, simian Vero E6 and LLC-
819 MK2, dog MDCK cells were maintained in complete Dulbecco's modified Eagle medium
820 (DMEM) (Gibco) supplemented with 10% foetal bovine serum and penicillin/streptomycin.
821 Human Caco-2 and Calu-3, simian LLC-MK2 cells were obtained from American Type
822 Culture Collection (ATCC; a gift from Nathalie Arhel for the latter); Vero E6 cells were
823 obtained from Sigma-Aldrich (a gift from Christine Chable-Bessia), HEK293T, A549, and
824 MDCK cells were gifts from Michael Malim's lab and Wendy Barclay's lab, Huh7 and
825 Huh7.5.1 cells have been described [74,75], respectively, and the latter provided by Raphaël
826 Gaudin. All cell lines were regularly screened for the absence of mycoplasma
827 contamination. When indicated, cells were treated with interferon (1000 U/mL, PBL
828 Interferon source) for 24h.
829 A549 cells (and Caco-2 cells, for the CRISPR screen) stably expressing ACE2 were
830 generated by transduction with RRL.sin.cPPT.SFFV.WPRE containing-vectors [30].
831 For CRISPR-Cas9-mediated gene disruption, Calu-3, Caco-2 and A549-ACE2, cells
832 stably expressing Cas9 or dCas9-VP64 were first generated by transduction with LX_311-

833 Cas9 or XPR_BRD109, respectively, followed by blasticidin selection at 10 μg/ml. WT
834 Cas9 activity was checked using the XPR_047 assay (a gift from David Root, Addgene
835 107145) and was always >80-90%. dCas9-VP64 activity was checked using the
836 pXPR_502 vector expressing sgRNA targeting IFITM3 and MX1 ISG promoters. Cells
837 were transduced with guide RNA expressing LentiGuide-Puro or XPR_502 (as indicated)
838 and selected with antibiotics for at least 10 days.
839
840 **Lentiviral production and transduction**
841 Lentiviral vector stocks were obtained by polyethylenimine (PEI; for LentiGuide vectors)
842 or Lipofectamine 3000 (Thermo Scientific; for XPR_502 vectors)-mediated multiple
843 transfections of 293T cells in 6-well plates with vectors expressing Gag-Pol, the miniviral
844 genome, the Env glycoprotein at a ratio of 1:1:0.5. The culture medium was changed 6h
845 post-transfection, and vector containing supernatants harvested 36 h later, filtered and
846 used directly or stored at -80°C. Transduction was performed by cell incubation with the
847 LV in the presence of polybrene (4 μg/mL) for a few hours. For LX_311-Cas9,
848 XPR_BRD109, RRL.sin.cPPT.SFFV/ACE2.WPRE, LentiGuide-Puro and XPR_502
849 transductions, spin infection was performed for 2h at 30°C and 1000g to improve
850 transduction efficiencies.
851
852 **CRISPR KO screens**
853 Vero E6, Caco-2-ACE2 and Calu-3 cells were spin infected for 2h at 1000g with LX_311-
854 Cas9 lentiviral vector at a high MOI and in the presence of polybrene (4 μg/mL). Blasticidin
855 selection was added 24-48h post transduction. Cells were grown to at least 120 million
856 cells (40-60 millions for the Calu-3) and transduced with lentiviral vectors coding the C.
857 *sabeus* sgRNAs [27] (for Vero E6), the Brunello library [32] (for Caco-2-ACE2) or the Gattinara
858 library [31] (for Calu-3), at MOI ~0.3-0.5. Puromycin selection was added 24-48h post
859 transduction and maintained for 10-15 days prior to proceeding to the screens. Cells were
860 re-amplified to at least the starting amounts prior to SARS-CoV-2 challenge at MOI 0.005.
861 The day of the viral challenge, 40 million cells were harvested, pelleted by centrifugation
862 and frozen down for subsequent gDNA extraction. Massive CPEs were observed 3-5

863 days post SARS-CoV-2 infection and cells were kept in culture for 11-13, 18-27, and 30-
864 34 days in total prior to harvest and gDNA extraction, for Vero E6, Caco-2-ACE2 and
865 Calu-3, respectively.
866
867 **CRISPRa screens**
868 Calu-3 cells were spin infected for 2h at 1000g with dCas9-VP64 (pXPR_BRD109)-
869 expressing lentiviral vectors at high MOI and in the presence of polybrene (4 μg/mL).
870 Blasticidin selection was added 24-48h post transduction and the cells were amplified.
871 120 million Calu-3-dCas9-VP64 cells were then transduced with the Calabrese library in
872 two biological replicates (for sublibrary A) or in one replicate (for sublibrary B) at a low
873 MOI (~0.3-0.5). 2.5 weeks later, 40 million cells were either challenged with SARS-CoV-
874 2 (MOI 0.005) or harvested and frozen down for subsequent gDNA extraction. Massive
875 CPEs were observed 3-5 days post SARS-CoV-2 infection and cells were kept in culture
876 for 11-17 days prior to harvest and gDNA extraction.
877
878 **Genomic DNA preparation and sequencing**
879 Genomic DNA (gDNA) was isolated using either the QIAamp DNA Blood Maxi kit
880 (Qiagen) or the NucleoSpin Blood XL kit (Macherey-Nagel), as per the manufacturer's
881 instructions. Isolated gDNAs were further prepared and cleaned up using a OneStep™
882 PCR Inhibitor Removal Kit according to manufacturer instructions (Zymo Research,
883 D6030). For PCR amplification, gDNA was divided into 100 µL reactions such that each
884 well had at most 10 µg of gDNA. Plasmid DNA (pDNA) was also included at a maximum
885 of 100 pg per well. Per 96 well plate, a master mix consisted of 150 µL DNA Polymerase
886 (Titanium Taq; Takara), 1 mL of 10x buffer, 800 µL of dNTPs (Takara), 50 µL of P5 stagger
887 primer mix (stock at 100 µM concentration), 500 µL of DMSO, and water to bring the final
888 volume to 4 mL. Each well consisted of 50 µL gDNA plus water, 40 µL PCR master mix,
889 and 10 µL of a uniquely barcoded P7 primer (stock at 5 µM concentration). PCR cycling
890 conditions were as follows: an initial 1 min at 95 °C; followed by 30 s at 94 °C, 30 s at
891 52.5 °C, 30 s at 72 °C, for 28 cycles; and a final 10 min extension at 72 °C. PCR primers
892 were synthesized at Integrated DNA Technologies (IDT). PCR products were purified with

893 Agencourt AMPure XP SPRI beads according to manufacturer's instructions (Beckman
894 Coulter, A63880). Prior to sequencing the sample was quantitated by qPCR and diluted
895 to 2nM. 5 μL of the sample was then further diluted and denatured with 5 μL 0.1N NaOH
896 and 490 μL HT1 buffer (Illumina). Samples were sequenced on a HiSeq2500 HighOutput
897 (Illumina) with a 5% spike-in of PhiX.
898

899 **Screen analysis**

900 For each published screen, corresponding authors provided raw read counts. For the
901 screens conducted in this paper, guide-level read counts were retrieved from sequencing
902 data. We log-normalized read counts using the following formula:

903 $$log - normalized\ reads\ per\ million\ for\ guide\ =\ log_2(\frac{number\ of\ reads\ per\ guide}{total\ reads\ in\ condition \times 1e6} + 1)$$

904 When applicable, we averaged lognorm values across conditions (Poirier, Daelemans,
905 Sanjana). We calculated log-fold changes for each condition relative to pDNA lognorm
906 values. If pDNA reads were not provided for the given screen, pDNA reads from a different
907 screen that used the same library were used (Puschnik analysis used Sanjana pDNA,
908 Zhang analysis used Poirier pDNA). Log-fold changes were used to calculate the
909 receiver-operator characteristic area under the curve values (ROC-AUC) for control
910 populations, where essential genes were treated as true positives and non-essential
911 genes were treated as true negatives. We define essential genes based on Hart et al.
912 2015 and non-essential genes based on Hart et al. 2014. For each condition in each
913 dataset, we fit a natural cubic spline between the control and infected conditions (Wei et
914 al. 2021). The degrees of freedom for each spline were fit using 10-fold cross-validation.
915 We calculated residuals from this spline and z-scored these values at the guide-level
916 (anchors package). We calculated gene-level z-scores by averaging across guides and
917 conditions, and p-values were combined across conditions using Fisher's method. Genes
918 were filtered by number of guides per gene, which was generally one guide fewer or
919 greater than the median number of genes per gene for that library (e.g. for Brunello
920 screens, which has a median of 4 guides per gene, we applied a filter of 3 to 5 guides per
921 gene). This guide-filtering step accounts for any missing values in the file compiling data

922 across all screens (all_screens_v3.xlsx). We then used these filtered gene-level z-scores
923 to rank the genes such that the rank one gene corresponded to the top resistance hit. The
924 files containing the guide-level and gene-level residual z-scores for each screen are being
925 deposited on Gene Expression Omnibus (GEO) (**Supplemental Files 1-5**). All code used
926 in this analysis can be found at: https://github.com/PriyankaRoy5/SARS-CoV-2-meta-
927 analysis.
928

929 **Wild-type and reporter SARS-CoV-2 production and infection**

930 The (wild-type) BetaCoV/France/IDF0372/2020 isolate was supplied by Pr. Sylvie van der
931 Werf and the National Reference Centre for Respiratory Viruses hosted by Institut
932 Pasteur (Paris, France). The patient sample from which strain
933 BetaCoV/France/IDF0372/2020 was isolated was provided by Dr. X. Lescure and Pr. Y.
934 Yazdanpanah from the Bichat Hospital, Paris, France. The mNeonGreen (mNG) [39] and
935 Nanoluciferase (NLuc) [55] reporter SARS-COV-2 were based on 2019-
936 nCoV/USA_WA1/2020 isolated from the first reported SARS-CoV-2 case in the USA, and
937 provided through World Reference Center for Emerging Viruses and Arboviruses
938 (WRCEVA), and UTMB investigator, Dr. Pei Yong Shi.
939 WT, mNG and NLuc reporter SARS-CoV-2 were amplified in Vero E6 cells (MOI 0.005)
940 in serum-free media. The supernatant was harvested at 48 h-72 h post infection when
941 cytopathic effects were observed, cell debris were removed by centrifugation, and
942 aliquots frozen down at -80°C. Viral supernatants were titrated by plaque assays in Vero
943 E6 cells. Typical titers were 3.10^6-3.10^7 plaque forming units (PFU)/ml.
944 Simian and human cell infections were performed at the indicated multiplicity of infection
945 (MOI; as calculated from titers in Vero E6 cells) in serum-free DMEM and 5% serum-
946 containing DMEM, respectively. The viral input was left for the duration of the experiment
947 (unless specified otherwise). The viral supernatants were frozen down at -80°C prior to
948 RNA extraction and quantification and/or titration by plaque assays on Vero E6 cells. The
949 cells were trypsinized and the percentage of cells expressing mNG was scored by flow
950 cytometry using a NovoCyte™ (ACEA Biosciences Inc.) after fixation in PBS1X-2% PFA,
951 or the cells were lysed in Passive Lysis buffer and NLuc activity measured inside the BSL-

952 3 facility, or lysed in RLT buffer (Qiagen) followed by RNA extraction and RT-qPCR
953 analysis, at the indicated time post-infection.
954
955 **Seasonal coronavirus production and infection**
956 HCoV-229E-Renilla was a gift from Volker Thiel [76] and was amplified for 5-7 days at 33°C
957 in Huh7.5.1 cells in 5% FCS-containing DMEM. HCoV-NL63 NR-470 was obtained
958 through BEI Resources, NIAID, NIH and was amplified for 5-7 days at 33°C in LLC-MK2
959 simian cells, in 2% FCS-containing DMEM. Viral stocks were harvested when cells
960 showed >50% CPEs. Viruses were titrated through $TCID_{50}$ in the cells used for their
961 amplification and typical titers were $1{,}8.10^9$ $TCID_{50}$/mL and 10^6 $TCID_{50}$/mL for HCoV-
962 229E-Renilla and HCoV-NL63, respectively. Infections of Calu-3 were performed at MOI
963 300 for HCoV-229E-Renilla (as measured on Huh7.5.1 cells) and MOI 0.1 for HCoV-NL63
964 (as measured on LLC-MK2 cells) and infection efficiency was analyzed 3 days later by
965 measuring Renilla activity or 5 days later by RT-qPCR for HCoV-229E-Renilla and HCoV-
966 NL63, respectively.
967
968 **MERS-CoV production and infection**
969 To produce MERS-CoV, HEK-293T cells were transfected with a bacmid containing a full-
970 length cDNA clone of the MERS-CoV genome (a king gift of Dr Luis Enjuanes; [77]) and
971 overlaid six hours later with Huh7 cells. After lysis of Huh7 cells, cell supernatants were
972 collected and the virus was further amplified on Huh7 cells. Viral stocks were aliquoted
973 and frozen down, and titrated by the $TCID_{50}$ method.
974 Calu-3 cells, seeded in 24-wells on glass coverslips (immunofluorescence) and in
975 duplicate in 48-wells (infectivity titrations), were inoculated with MERS-CoV at an MOI of
976 0.3. Sixteen hours after inoculation, coverslips were fixed by incubation in 3%
977 paraformaldehyde for 20 minutes, and stored in PBS at 4°C until immunolabeling was
978 performed. Supernatant was collected from the infected cells in the 48-wells and stored
979 at -80°C until infectivity titrations were performed. Coverslips were further processed for
980 immunolabeling of the infected cells. Briefly, cells were permeabilized by incubation with
981 0.4% Triton X-100 for 5 minutes, and were then blocked by incubation for 30 minutes with

982 5% goat serum (GS) in PBS. Infected cells were labelled with a mixture of the mouse
983 monoclonal antibody J2 against dsRNA (Scicons, diluted 1:400) and a rabbit polyclonal
984 antibody directed against the spike protein (Sino Biological Inc, diluted 1:500) in PBS
985 supplemented with 5% GS for 30 minutes at room temperature. They were washed three
986 times with PBS and then incubated for 30 minutes with Alexa-488-conjugated donkey
987 anti-mouse IgG and Alexa594-conjugated goat anti-rabbit IgG secondary antibodies (both
988 from Jackson Immunoresearch) in 5% GS in PBS supplemented with 1 µg/ml DAPI (4′,6-
989 diamidino-2-phenylindole). Coverslips were then rinsed four times with PBS, once in
990 MilliQ water and mounted on microscope slides in Mowiol 4-88-containing medium.
991 Images were acquired on an Evos M5000 imaging system (Thermo Fisher Scientific)
992 equipped with light cubes for DAPI, GFP and TX-RED, and a 10x objective. For each
993 coverslip, ten 8-bit images of each channel were acquired. The total number of cells was
994 determined by counting the nuclei. Infected cells, defined as positive for dsRNA or spike
995 immunolabeling, were counted, and the percentage of infected cells was calculated.
996 About 10,000 to 20,000 cells were counted per condition in each experiment using
997 homemade macros running in ImageJ. For the infectivity titrations, Huh7 cells, seeded in
998 96 well plates, were inoculated with 100 µl of 1/10 serially diluted supernatants. Cells
999 were incubated with the virus dilutions for 5 days at 37°C. Then, the 50% tissue culture
1000 infectious dose ($TCID_{50}$) was determined by assessing the CPEs in each well by light
1001 microscopy and the 50% and point was calculated according to the method of Reed and
1002 Muench [78].
1003

1004 **IAV-NLuc production and infection**

1005 The A/Victoria/3/75 virus carrying a NanoLuciferase reporter gene generation and
1006 production have been described [73]. Viruses were amplified on MDCK cells cultured in
1007 serum-free DMEM containing 0.5 µg/mL L-1-p-Tosylamino-2-phenylethyl chloromethyl
1008 ketone (TPCK)-treated trypsin (Sigma–Aldrich). Stocks were titrated by plaque assays on
1009 MDCK cells.
1010 IAV-NLuc challenges were performed in quadruplicates in 96-well plates, in serum-free
1011 DMEM for 1 h and the medium was subsequently replaced with DMEM containing 10%

1012 foetal bovine serum. The cells were lysed 10h later and NanoLuc activity was measured
1013 with the Nano-Glo assay system (Promega), and luminescence was detected using a
1014 plate reader (Infinite 200 PRO; Tecan).
1015

1016 **SARS-CoV-2 internalization assay**

1017 Calu-3 cells were incubated with SARS-CoV-2 at an MOI of 5 for 2h at 37°C, were washed
1018 twice with PBS and then treated with Subtilisin A (400 µg/mL) in Subtilisin A buffer (10
1019 mM Tris/HCl (pH 8.0), 150 mM NaCl, 5 mM $CaCl_2$)) in order to get rid of the cell surface-
1020 bound viruses, prior to lysis in 350 µL RLT buffer, RNA extraction using the RNeasy kit
1021 according the manufacturer's instructions (Qiagen) and RdRp RT-qPCR to measure the
1022 relative amounts of internalized viruses.
1023

1024 **Spike pseudotype production**

1025 293T cells were seeded in a 6 well plate previously coated with poly-Lysine (Sigma-
1026 Aldrich) and, 1 day later, transfected with 5 µg of an expression plasmid coding either
1027 VSV-G (pMD.G) or SARS-CoV-2 Spike del19 (pcDNA3.1_spike_del19) using
1028 Lipofectamine 2000 (Thermo Scientific). The culture medium was replaced after 6h. Cells
1029 were infected 24h post-transfection with VSVΔG-GFP-Firefly Luciferase [41] at a MOI of 5
1030 for 1h at 37°C and subsequently rinsed 3 times with PBS. The medium was replaced with
1031 5%FCS-supplemented DMEM complemented with a mouse monoclonal anti-VSV-G
1032 antibody (CliniSciences, clone 8G5F11, final concentration 1 µg/mL) to neutralize residual
1033 viral input, as described [79]. Cell supernatants containing pseudotyped VSV viruses were
1034 harvested 24h later, spun at 1000 g for 10 min and stored at -80°C.
1035

1036 **RNA quantification**

1037 3-5 x 10^5 cells infected or not with SARS-CoV-2 or HCoV-NL63 were harvested and total
1038 RNA was extracted using the RNeasy kit (Qiagen) employing on-column DNase
1039 treatment, according to the manufacturer's instructions. 50-125 ng of total RNAs were
1040 used to generate cDNAs. To quantify SARS-CoV-2 RNAs, the cDNAs were analyzed by
1041 qPCR using published RdRp primers and probe [80], as follow: RdRp_for 5'-

1042 GTGARATGGTCATGTGTGGCGG-3', RdRp_rev 5'-
1043 CAAATGTTAAAAACACTATTAGCATA-3', and RdRp_probe 5'-FAM-
1044 CAGGTGGAACCTCATCAGGAGATGC-TAMRA-3'). To quantify HCoV-NL63 RNAs, the
1045 cDNAs were analyzed by qPCR using published primers and probe (Carbajo-Lozoya et
1046 al., 2012), as follow: NL-63F2 5′-CTTCTGGTGACGCTAGTACAGCTTAT-3′, NL-63R2
1047 5′-AGACGTCGTTGTAGATCCCTAACAT-3′, and NL-63 probe 5′-FAM-
1048 CAGGTTGCTTAGTGTCCCATCAGATTCAT-TAMRA-3′ [81]. For relative levels of
1049 expression of the genes of interest, the following TaqMan gene expression assays were
1050 used (ThermoFisher Scientific): *ACTB* (Hs99999903_m1), *GAPDH* (Hs99999905_m1),
1051 *AP1B1* (Hs00153906_m1), *AP1G1* (Hs00964419_m1), *AAGAB* (Hs01027607_m1),
1052 *KMT2C* (Hs01005521_m1), *EP300* (Hs00914205_m1), *ATP8B1* (Hs00900656_m1),
1053 *PLAGL1* (Hs00414677_m1), *MUC4* (Hs00366414_m1), *MUC21* (Hs01379324_g1),
1054 *MUC1* (Hs00159357_m1), *IL6R* (Hs01075664_m1), *LYN* (Hs00176719_m1), *TEAD3*
1055 (Hs00243231_m1) and *CD44* (Hs01075862_m1). qPCR reactions were performed in
1056 triplicate, in universal PCR master mix using 900 nM of each primer and 250 nM probe
1057 or the indicated Taqmans. After 10 min at 95°C, reactions were cycled through 15 s at
1058 95°C followed by 1 min at 60°C for 40 repeats. Triplicate reactions were run according to
1059 the manufacturer's instructions using a ViiA7 Real Time PCR system (ThermoFisher
1060 Scientific). pRdRp and pNL63 (which respectively contains fragments amplified from
1061 SARS-CoV-2- and NL63-infected cell RNAs using primers RdRp_for and RdRp_rev, and
1062 NL-63F2 and NL-63R2, cloned into pPCR-Blunt II-TOPO) was diluted in 20 ng/ml salmon
1063 sperm DNA to generate a standard curve to calculate relative cDNA copy numbers and
1064 confirm the assay linearity (detection limit: 10 molecules of RdRp per reaction).
1065

1066 **ACE2 staining using Spike RBD-mFc recombinant protein and flow cytometry**
1067 **analysis**

1068 The SARS-CoV-2 Spike RBD sequence used here as a soluble tagged exofacial ligand
1069 for ACE2, was obtained from RNA extracted from a patient nasopharyngeal sample
1070 collected in Montpellier University hospital during Spring 2020 and a gift from Vincent
1071 Foulongne [82] (RBD sequence GenBank accession number MT787505.1). The predicted

1072 N-terminal signal peptide of the spike protein (amino acid 1-14) was fused to the RBD
1073 sequence (amino acid 319-541) and C-terminally tagged with a mouse IgG1 Fc fragment.
1074 The RBD-mFc fusion sequence was then cloned into a pCSI vector for expression in
1075 mammalian cells, as previously described (Giovannini et al., 2013). The pCSI-SpikeRBD
1076 expression vector was transfected in HEK293T cells using the PEIpro® transfection
1077 reagent. Cells were washed 6h post transfection and grown for an additional 72-96h in
1078 serum-free Optipro medium (Invitrogen) supplemented with glutamine and non-essential
1079 amino acids. Conditioned medium was then harvested, filtered through 0.45 μm filters
1080 and concentrated 100-fold by centrifugation at 3600 rpm at 4°C on 10 kDA cut-off Amicon
1081 Ultra-15 concentrators. Samples were aliquoted and stored at -20°C until further use.
1082 For ACE2 labelling, cells were harvested and incubated 20 min at 37°C in FACS buffer
1083 (PBS1X-2% BSA) containing a 1/20 dilution of Spike RBD-mFc followed by secondary
1084 anti-mouse Alexa-488 incubation and several washes in FACS buffer. Flow cytometry
1085 was performed using the NovoCyte™ (ACEA Biosciences Inc.).
1086
1087 **Immunoblot analysis**
1088 Cells were lysed in lysis buffer (10 mM TRIS 1M pH7.6, NaCl 150 mM, Triton X100 1%,
1089 EDTA 1 mM, deoxycholate 0,1%) supplemented with sample buffer (50 mM Tris-HCl pH
1090 6.8, 2% SDS, 5% glycerol, 100 mM DTT, 0.02% bromophenol blue), resolved by SDS-
1091 PAGE and analyzed by immunoblotting using primary antibodies against ACE2
1092 (ProteinTech 21115-1-P) and Actin (Sigma-Aldrich A1978), followed by HRP-conjugated
1093 anti-rabbit or anti-mouse immunoglobulin antibodies and chemiluminescence Clarity or
1094 Clarity max substrate (Bio-Rad). A Bio-Rad ChemiDoc imager was used.
1095
1096 **Analysis of scRNAseq data**
1097 For scRNaseq analysis, Seurat objects were downloaded from figshare:
1098 (https://doi.org/10.6084/m9.figshare.12436517.v2; [40]). Cell identities and CRISPR hits
1099 were selected and plotted using the DotPlot function in Seurat [40].
1100
1101

1102 **Data availability**

1103 The datasets generated during and/or analyzed during the current study are being
1104 deposited with GEO and are additionally available from the corresponding authors on
1105 reasonable request.

1106

1107 **Requests for materials**

1108 Requests for material should be addressed to Caroline Goujon or John Doench at the
1109 corresponding address above, or to Addgene for the plasmids with an Addgene number.

1110

1111 **Acknowledgements**

1112 We are thankful to Sylvie Van de Werf from the French National Reference Centre for
1113 Respiratory Viruses (Pasteur Institute) for providing us with SARS-CoV-2
1114 BetaCoV/France/IDF0372/2020 (isolated by Dr. X. Lescure and Pr. Y. Yazdanpanah,
1115 Bichat hospital), to the World Reference Center for Emerging Viruses and Arboviruses
1116 (WRCEVA) and UTMB investigator, Dr. Pei Yong Shi, for the mNeon Green and NanoLuc
1117 reporter SARS-CoV-2; to Volker Thiel for Renilla reporter HCoV-229E; to BEI Resources,
1118 NIAID, NIH for providing us with HCoV-NL63. We wish to thank Raphaël Gaudin, Lucile
1119 Espert, Véronique Hebmann, Christine Chable-Bessia, Lise Chauveau, Bruno
1120 Beaumelle, Nathalie Arhel, Marc Sitbon, Vincent Foulongne, and Raffaele De Francesco
1121 for the generous provision of reagents, and we are thankful to María Moriel-Carretero
1122 and Laura Picas for helpful discussions. We are grateful to Christine Chable-Bessia and
1123 all CEMIPAI BSL-3 facility members for setting up excellent working conditions for SARS-
1124 CoV-2 handling.

1125 This work was supported by the French National Research Agency ANR under the ANR-
1126 RA COVID program (ANR-20-COV6-0001, CRISPR-TARGET-CoV, to CG), the
1127 European Research Council (ERC) under the European Union's Horizon 2020 research
1128 and innovation programme (grant agreement 759226, ANTIViR, to CG), the Institut
1129 National de la Santé et de la Recherche Médicale (INSERM) (to CG), the 'Fondation
1130 CNRS' (to CG & OM), institutional funds from the Centre National de la Recherche
1131 Scientifique (CNRS) and Institut des Sciences Biologiques du CNRS (INSB) (to CG and

OM), 3-year PhD studentships from the Ministry of Higher Education and Research (to AR, BB, and JM), a 4th year PhD funding from the Fondation pour la Recherche Médicale (to BB), NIAID R21AI157835 (to JGD), the COVID program from CNRS (to L.D.). We acknowledge the imaging facility MRI, member of the national infrastructure France-BioImaging supported by the French National Research Agency (ANR-10-INBS-04) and the CEMIPAI BSL-3 facility.

Author contributions

A.R., P.R., J.G.D. and C.G. conceived the study; A.R. and C.G. designed the experiments; A.R. and C.G. performed the CRISPR screens; P.R., M.H., P.DW. and J.G.D. performed the computational analysis; A.R., B.B., A.L.C.V., L.D., O.M. and C.G. performed the BSL-2 and BSL-3 experiments; Y.R., M.T., M.A.A. and Y.L. provided technical help; D.G. provided Spike RBD-mFc for ACE2 staining; F.G.G, J.M., M.W. participated in data interpretation. J.G.D. and C.G. provided overall supervision along with S.B. and J.D.; A.R., P.R., J.G.D. and C.G. wrote the manuscript with input from all authors.

Competing interests

J.G.D. consults for Agios, Microsoft Research, Phenomic AI, BioNTech, and Pfizer; JGD consults for and has equity in Tango Therapeutics. J.G.D.'s interests were reviewed and are managed by the Broad Institute in accordance with its conflict of interest policies. The other authors declare no competing interests.

1160 **References**

1161 1. Drosten, C. *et al.* Identification of a Novel Coronavirus in Patients with Severe Acute
1162 Respiratory Syndrome. *N Engl J Med* **348**, 1967–1976 (2003).
1163 2. Peiris, J. *et al.* Coronavirus as a possible cause of severe acute respiratory syndrome. *The*
1164 *Lancet* **361**, 1319–1325 (2003).
1165 3. Zhong, N. *et al.* Epidemiology and cause of severe acute respiratory syndrome (SARS) in
1166 Guangdong, People's Republic of China, in February, 2003. *The Lancet* **362**, 1353–1358
1167 (2003).
1168 4. Zaki, A. M., van Boheemen, S., Bestebroer, T. M., Osterhaus, A. D. M. E. & Fouchier, R. A.
1169 M. Isolation of a Novel Coronavirus from a Man with Pneumonia in Saudi Arabia. *N Engl J*
1170 *Med* **367**, 1814–1820 (2012).
1171 5. Zhou, F. *et al.* Clinical course and risk factors for mortality of adult inpatients with COVID-19
1172 in Wuhan, China: a retrospective cohort study. *The Lancet* **395**, 1054–1062 (2020).
1173 6. van der Hoek, L. Human coronaviruses: what do they cause? *Antivir. Ther. (Lond.)* **12**, 651–
1174 658 (2007).
1175 7. Xiao, F. *et al.* Evidence for Gastrointestinal Infection of SARS-CoV-2. *Gastroenterology* **158**,
1176 1831-1833.e3 (2020).
1177 8. Hoffmann, M. *et al.* SARS-CoV-2 Cell Entry Depends on ACE2 and TMPRSS2 and Is
1178 Blocked by a Clinically Proven Protease Inhibitor. *Cell* **181**, 271-280.e8 (2020).
1179 9. Hofmann, H. *et al.* Human coronavirus NL63 employs the severe acute respiratory
1180 syndrome coronavirus receptor for cellular entry. *Proc Natl Acad Sci U S A* **102**, 7988–7993
1181 (2005).
1182 10. Li, W. *et al.* Angiotensin-converting enzyme 2 is a functional receptor for the SARS
1183 coronavirus. *Nature* **426**, 450–454 (2003).
1184 11. Wu, K., Li, W., Peng, G. & Li, F. Crystal structure of NL63 respiratory coronavirus receptor-

1185 binding domain complexed with its human receptor. *Proc Natl Acad Sci U S A* **106**, 19970–
1186 19974 (2009).
1187 12. Zhou, P. *et al.* A pneumonia outbreak associated with a new coronavirus of probable bat
1188 origin. *Nature* **579**, 270–273 (2020).
1189 13. Matsuyama, S. *et al.* Efficient activation of the severe acute respiratory syndrome
1190 coronavirus spike protein by the transmembrane protease TMPRSS2. *J. Virol.* **84**, 12658–
1191 12664 (2010).
1192 14. Huang, I.-C. *et al.* SARS coronavirus, but not human coronavirus NL63, utilizes cathepsin L
1193 to infect ACE2-expressing cells. *J. Biol. Chem.* **281**, 3198–3203 (2006).
1194 15. Ou, X. *et al.* Characterization of spike glycoprotein of SARS-CoV-2 on virus entry and its
1195 immune cross-reactivity with SARS-CoV. *Nat Commun* **11**, 1620 (2020).
1196 16. Simmons, G. *et al.* Inhibitors of cathepsin L prevent severe acute respiratory syndrome
1197 coronavirus entry. *Proc. Natl. Acad. Sci. U.S.A.* **102**, 11876–11881 (2005).
1198 17. Yeager, C. L. *et al.* Human aminopeptidase N is a receptor for human coronavirus 229E.
1199 *Nature* **357**, 420–422 (1992).
1200 18. Raj, V. S. *et al.* Dipeptidyl peptidase 4 is a functional receptor for the emerging human
1201 coronavirus-EMC. *Nature* **495**, 251–254 (2013).
1202 19. Bertram, S. *et al.* TMPRSS2 activates the human coronavirus 229E for cathepsin-
1203 independent host cell entry and is expressed in viral target cells in the respiratory
1204 epithelium. *J Virol* **87**, 6150–6160 (2013).
1205 20. Gierer, S. *et al.* The spike protein of the emerging betacoronavirus EMC uses a novel
1206 coronavirus receptor for entry, can be activated by TMPRSS2, and is targeted by
1207 neutralizing antibodies. *J Virol* **87**, 5502–5511 (2013).
1208 21. V'kovski, P., Kratzel, A., Steiner, S., Stalder, H. & Thiel, V. Coronavirus biology and
1209 replication: implications for SARS-CoV-2. *Nat Rev Microbiol* (2020) doi:10.1038/s41579-
1210 020-00468-6.

1211 22. Irving, A. T., Ahn, M., Goh, G., Anderson, D. E. & Wang, L.-F. Lessons from the host
1212 defences of bats, a unique viral reservoir. *Nature* **589**, 363–370 (2021).
1213 23. Baggen, J. *et al.* Genome-wide CRISPR screening identifies TMEM106B as a proviral host
1214 factor for SARS-CoV-2. *Nat Genet* (2021) doi:10.1038/s41588-021-00805-2.
1215 24. Daniloski, Z. *et al.* Identification of Required Host Factors for SARS-CoV-2 Infection in
1216 Human Cells. *Cell* **184**, 92-105.e16 (2021).
1217 25. Schneider, W. M. *et al.* Genome-Scale Identification of SARS-CoV-2 and Pan-coronavirus
1218 Host Factor Networks. *Cell* **184**, 120-132.e14 (2021).
1219 26. Wang, R. *et al.* Genetic Screens Identify Host Factors for SARS-CoV-2 and Common Cold
1220 Coronaviruses. *Cell* **184**, 106-119.e14 (2021).
1221 27. Wei, J. *et al.* Genome-wide CRISPR Screens Reveal Host Factors Critical for SARS-CoV-2
1222 Infection. *Cell* **184**, 76-91.e13 (2021).
1223 28. Zhu, Y. *et al.* A genome-wide CRISPR screen identifies host factors that regulate SARS-
1224 CoV-2 entry. *Nat Commun* **12**, 961 (2021).
1225 29. Szklarczyk, D. *et al.* The STRING database in 2021: customizable protein-protein networks,
1226 and functional characterization of user-uploaded gene/measurement sets. *Nucleic Acids*
1227 *Res* **49**, D605–D612 (2021).
1228 30. Rebendenne, A. *et al.* SARS-CoV-2 triggers an MDA-5-dependent interferon response
1229 which is unable to control replication in lung epithelial cells. *J Virol* (2021)
1230 doi:10.1128/JVI.02415-20.
1231 31. DeWeirdt, P. C. *et al.* Genetic screens in isogenic mammalian cell lines without single cell
1232 cloning. *Nat Commun* **11**, 752 (2020).
1233 32. Sanson, K. R. *et al.* Optimized libraries for CRISPR-Cas9 genetic screens with multiple
1234 modalities. *Nat Commun* **9**, 5416 (2018).
1235 33. Camargo, S. M. R., Vuille-Dit-Bille, R. N., Meier, C. F. & Verrey, F. ACE2 and gut amino
1236 acid transport. *Clin Sci (Lond)* **134**, 2823–2833 (2020).

1237 34. Di Paola, M. *et al.* SLC6A14 Is a Genetic Modifier of Cystic Fibrosis That Regulates
1238 Pseudomonas aeruginosa Attachment to Human Bronchial Epithelial Cells. *mBio* **8**, (2017).
1239 35. Pfaender, S. *et al.* LY6E impairs coronavirus fusion and confers immune control of viral
1240 disease. *Nat Microbiol* **5**, 1330–1339 (2020).
1241 36. Chatterjee, M., van Putten, J. P. M. & Strijbis, K. Defensive Properties of Mucin
1242 Glycoproteins during Respiratory Infections-Relevance for SARS-CoV-2. *mBio* **11**, (2020).
1243 37. McAuley, J. L. *et al.* The cell surface mucin MUC1 limits the severity of influenza A virus
1244 infection. *Mucosal Immunology* **10**, 1581–1593 (2017).
1245 38. Plante, J. A. *et al.* Mucin 4 Protects Female Mice from Coronavirus Pathogenesis. *bioRxiv*
1246 2020.02.19.957118 (2020) doi:10.1101/2020.02.19.957118.
1247 39. Xie, X. *et al.* An Infectious cDNA Clone of SARS-CoV-2. *Cell Host Microbe* **27**, 841-848.e3
1248 (2020).
1249 40. Chua, R. L. *et al.* COVID-19 severity correlates with airway epithelium–immune cell
1250 interactions identified by single-cell analysis. *Nature Biotechnology* **38**, 970–979 (2020).
1251 41. Rentsch, M. B. & Zimmer, G. A Vesicular Stomatitis Virus Replicon-Based Bioassay for the
1252 Rapid and Sensitive Determination of Multi-Species Type I Interferon. *PLoS ONE* **6**, (2011).
1253 42. Schmidt, F. *et al.* Measuring SARS-CoV-2 neutralizing antibody activity using pseudotyped
1254 and chimeric viruses. *J Exp Med* **217**, (2020).
1255 43. Stanifer, M. L. *et al. Critical role of type III interferon in controlling SARS-CoV-2 infection,*
1256 *replication and spread in primary human intestinal epithelial cells*.
1257 http://biorxiv.org/lookup/doi/10.1101/2020.04.24.059667 (2020)
1258 doi:10.1101/2020.04.24.059667.
1259 44. Jordan, A. R., Racine, R. R., Hennig, M. J. P. & Lokeshwar, V. B. The Role of CD44 in
1260 Disease Pathophysiology and Targeted Treatment. *Front. Immunol.* **6**, (2015).
1261 45. Ponta, H., Sherman, L. & Herrlich, P. A. CD44: from adhesion molecules to signalling
1262 regulators. *Nat Rev Mol Cell Biol* **4**, 33–45 (2003).

1263 46. Vega-Benedetti, A. F. *et al.* PLAGL1: an important player in diverse pathological processes.
1264 *J Appl Genet* **58**, 71–78 (2017).
1265 47. Mihara, M., Hashizume, M., Yoshida, H., Suzuki, M. & Shiina, M. IL-6/IL-6 receptor system
1266 and its role in physiological and pathological conditions. *Clinical Science* **122**, 143–159
1267 (2011).
1268 48. Han, Z. *et al.* YAP/TEAD3 signal mediates cardiac lineage commitment of human-induced
1269 pluripotent stem cells. *J Cell Physiol* **235**, 2753–2760 (2020).
1270 49. Imajo, M., Ebisuya, M. & Nishida, E. Dual role of YAP and TAZ in renewal of the
1271 intestinal epithelium. *Nat Cell Biol* **17**, 7–19 (2015).
1272 50. Brodie, E. J., Infantino, S., Low, M. S. Y. & Tarlinton, D. M. Lyn, Lupus, and (B)
1273 Lymphocytes, a Lesson on the Critical Balance of Kinase Signaling in Immunity. *Front*
1274 *Immunol* **9**, 401 (2018).
1275 51. Li, X. *et al.* Lyn regulates inflammatory responses in Klebsiella pneumoniae infection via the
1276 p38/NF-κB pathway. *Eur J Immunol* **44**, 763–773 (2014).
1277 52. Li, M. Y. *et al.* Lyn kinase regulates egress of flaviviruses in autophagosome-derived
1278 organelles. *Nat Commun* **11**, 5189 (2020).
1279 53. Dhar, P. & McAuley, J. The Role of the Cell Surface Mucin MUC1 as a Barrier to Infection
1280 and Regulator of Inflammation. *Front Cell Infect Microbiol* **9**, 117 (2019).
1281 54. Linden, S. K., Sutton, P., Karlsson, N. G., Korolik, V. & McGuckin, M. A. Mucins in the
1282 mucosal barrier to infection. *Mucosal Immunology* **1**, 183–197 (2008).
1283 55. Xie, X. *et al.* A nanoluciferase SARS-CoV-2 for rapid neutralization testing and screening of
1284 anti-infective drugs for COVID-19. *Nature Communications* **11**, 5214 (2020).
1285 56. Funk, C. J. *et al.* Infection of human alveolar macrophages by human coronavirus strain
1286 229E. *J Gen Virol* **93**, 494–503 (2012).
1287 57. Stiewe, T. & Pützer, B. M. p73 in apoptosis. *Apoptosis* **6**, 447–452 (2001).
1288 58. Urist, M., Tanaka, T., Poyurovsky, M. V. & Prives, C. p73 induction after DNA damage is

1289 regulated by checkpoint kinases Chk1 and Chk2. *Genes Dev* **18**, 3041–3054 (2004).
1290 59. Zaika, E. *et al.* p73 protein regulates DNA damage repair. *FASEB J* **25**, 4406–4414 (2011).
1291 60. Long, Z. *et al.* Inhibition of hepatocyte nuclear factor 1b induces hepatic steatosis through
1292 DPP4/NOX1-mediated regulation of superoxide. *Free Radical Biology and Medicine* **113**,
1293 71–83 (2017).
1294 61. Katsuoka, F. & Yamamoto, M. Small Maf proteins (MafF, MafG, MafK): History, structure
1295 and function. *Gene* **586**, 197–205 (2016).
1296 62. Kumar, N., Mishra, B., Mehmood, A., Mohammad Athar, & M Shahid Mukhtar. Integrative
1297 Network Biology Framework Elucidates Molecular Mechanisms of SARS-CoV-2
1298 Pathogenesis. *iScience* **23**, 101526 (2020).
1299 63. Biering, S. B. *et al.* Genome-wide, bidirectional CRISPR screens identify mucins as critical
1300 host factors modulating SARS-CoV-2 infection. *bioRxiv* 2021.04.22.440848 (2021)
1301 doi:10.1101/2021.04.22.440848.
1302 64. Nakatsu, F., Hase, K. & Ohno, H. The Role of the Clathrin Adaptor AP-1: Polarized Sorting
1303 and Beyond. *Membranes (Basel)* **4**, 747–763 (2014).
1304 65. Gulbranson, D. R. *et al.* AAGAB Controls AP2 Adaptor Assembly in Clathrin-Mediated
1305 Endocytosis. *Developmental Cell* **50**, 436-446.e5 (2019).
1306 66. Paulusma, C. C. & Oude Elferink, R. P. J. The type 4 subfamily of P-type ATPases, putative
1307 aminophospholipid translocases with a role in human disease. *Biochimica et Biophysica*
1308 *Acta (BBA) - Molecular Basis of Disease* **1741**, 11–24 (2005).
1309 67. Stukalov, A. *et al.* Multilevel proteomics reveals host perturbations by SARS-CoV-2 and
1310 SARS-CoV. *Nature* 1–7 (2021) doi:10.1038/s41586-021-03493-4.
1311 68. Li, Y. E. *et al.* TMEM41B and VMP1 are scramblases and regulate the distribution of
1312 cholesterol and phosphatidylserine. *J Cell Biol* **220**, (2021).
1313 69. Rosas, I. O. *et al.* Tocilizumab in Hospitalized Patients with Severe Covid-19 Pneumonia.
1314 *New England Journal of Medicine* **384**, 1503–1516 (2021).

1315 70. Valyaeva, A. A., Zharikova, A. A., Kasianov, A. S., Vassetzky, Y. S. & Sheval, E. V.
1316 Expression of SARS-CoV-2 entry factors in lung epithelial stem cells and its potential
1317 implications for COVID-19. *Scientific Reports* **10**, 17772 (2020).
1318 71. Sanjana, N. E., Shalem, O. & Zhang, F. Improved vectors and genome-wide libraries for
1319 CRISPR screening. *Nat Methods* **11**, 783–784 (2014).
1320 72. Shalem, O. *et al.* Genome-scale CRISPR-Cas9 knockout screening in human cells. *Science*
1321 **343**, 84–87 (2014).
1322 73. Doyle, T. *et al.* The interferon-inducible isoform of NCOA7 inhibits endosome-mediated viral
1323 entry. *Nat Microbiol* **3**, 1369–1376 (2018).
1324 74. Nakabayashi, H., Taketa, K., Miyano, K., Yamane, T. & Sato, J. Growth of human hepatoma
1325 cells lines with differentiated functions in chemically defined medium. *Cancer Res* **42**, 3858–
1326 3863 (1982).
1327 75. Zhong, J. *et al.* Robust hepatitis C virus infection in vitro. *Proc Natl Acad Sci U S A* **102**,
1328 9294–9299 (2005).
1329 76. van den Worm, S. H. E. *et al.* Reverse genetics of SARS-related coronavirus using vaccinia
1330 virus-based recombination. *PLoS One* **7**, e32857 (2012).
1331 77. Almazán, F. *et al.* Engineering a Replication-Competent, Propagation-Defective Middle East
1332 Respiratory Syndrome Coronavirus as a Vaccine Candidate. *mBio* **4**, (2013).
1333 78. REED, L. J. & MUENCH, H. A SIMPLE METHOD OF ESTIMATING FIFTY PER CENT
1334 ENDPOINTS12. *American Journal of Epidemiology* **27**, 493–497 (1938).
1335 79. Condor Capcha, J. M. *et al.* Generation of SARS-CoV-2 Spike Pseudotyped Virus for Viral
1336 Entry and Neutralization Assays: A 1-Week Protocol. *Front Cardiovasc Med* **7**, 618651
1337 (2020).
1338 80. Corman, V. M. *et al.* Detection of 2019 novel coronavirus (2019-nCoV) by real-time RT-
1339 PCR. *Euro Surveill* **25**, (2020).
1340 81. Carbajo-Lozoya, J. *et al.* Replication of human coronaviruses SARS-CoV, HCoV-NL63 and

1341 HCoV-229E is inhibited by the drug FK506. *Virus Res* **165**, 112–117 (2012).

1342 82. Veyrenche, N. *et al.* Diagnosis value of SARS-CoV-2 antigen/antibody combined testing

1343 using rapid diagnostic tests at hospital admission. *J Med Virol* **93**, 3069–3076 (2021).

1344

1345

1346 **Table 1. Properties of SARS-CoV-2 host factor screens assayed by cell viability.**
1347 For each library, the number of unique guides per gene is indicated in parentheses. The essential gene QC
1348 serves as a metric for screen quality (see Methods) in the untreated arm, when applicable; the number of
1349 days post-library introduction until the end of the experiment is written after the semicolon.
1350

Study	Cell line	Library (#guides/gene)	Viral isolate	Essential gene QC (ROC-AUC; #days)
Wei, Wilen	Vero E6	C. sabeus (4)	USA-WA1/2020	0.82; 16-18 days
This study	Vero E6	C. sabeus (4)	BetaCoV/France/ IDF0372/2020	0.84; 20-24 days
Daniloski, Sanjana	A549-ACE2	GeCKO (6)	USA-WA1/2020	0.62; 18 days
Zhu, Zhang	A549-ACE2	Brunello (4)	nCoV-SH01	0.68; 14+ days
Baggen, Daelemans	Huh7	Brunello (4)	Belgium/GHB-03021/2020	0.78; 44 days
Schneider, Poirier	Huh7.5	Brunello (4)	USA-WA1/2020	0.92; 12-21 days
Wang, Puschnik	Huh7.5.1-ACE2-TMPRSS2	GeCKO (6)	USA-WA1/2020	0.56; 19 days
This study	Caco-2-ACE2	Brunello (4)	BetaCoV/France/ IDF0372/2020	0.71; 19 days
This study	Calu-3	Gattinara (2)	BetaCoV/France/ IDF0372/2020	0.84; 13-30 days
This study	Calu-3	Calabrese (6)	BetaCoV/France/ IDF0372/2020	n/a; 17-19 days

1351

1352 **Table 2. sgRNA sequences used for CRISPR KO perturbations**

Gene	sgRNA sequence
CTRL g1	AGCACGTAATGTCCGTGGAT
CTRL g2	CAATCGGCGACGTTTTAAAT
ACE2 g1	TCCTGTGCAGATATTACACA
ACE2 g2	ACAGTTTAGACTACAATGAG
TMPRSS2 g1	GTCCAGAACGTCCACGTGTG
TMPRSS2 g2	CGGATGCACCTCGTAGACAG
AP1B1 g1	TTGTGGGCGAGTACGCGGAA
AP1B1 g2	ACTGTGGGTTCAGATCGAGC
AP1G1 g1	GTAAATGGGAATAATATCCG
AP1G1 g2	TGTTCAATAAGAAACGACCC
AAGAB g1	AGCAGACATCAATCTATGTG
AAGAB g2	AAGCCCTGAATGCCAATGTG
KMT2C g1	ATTCAGACATTAGGCCATCG
KMT2C g2	CCCATGCGACGACCTCCCCA
KDM6A g1	CCTAGCAATTCAGTAACACA
KDM6A g2	CTGGTAAGTCTCACCTTCCG
KMT2D g1	GGTGGAAATTCCCGCCAACG
KMT2D g2	CTTCCCTATGGGACTCAACG
ARID2 g1	GTAAGCCAGCCAGCTCAACA
ARID2 g2	GCAGTCTCCATTACACACAG
DYRK1A g1	TGAGAAACACCAATTTCCGA
DYRK1A g2	TTCAACCAAAATACACCCGA
VPS72 g1	TTCTACCAGACGACTTATGG
VPS72 g2	GCCTCGAAAGGTCAACACCC
PBRM1 g1	TTGAAAATAATCGCTACCGT
PBRM1 g2	AGGAGTTGTCGGAATAACCA
EP300 g1	GGTACGACTAGGTACAGGCG
EP300 g2	TTCTTCATTGTGCGACAGTG
SRRD g1	AGGGAAACGGAGTATTCGCG
SRRD g2	GCATCTTGACTCATTGCCAG
RAD54L2 g1	GTTCCTTTACGATAACCTAG
RAD54L2 g2	GTATACCCGACATACTGCCT
PCBD1 g1	CTTTGGGTTCATGACAAGAG
PCBD1 g2	ACACGTTAAACCATTCAGGA
ARID1A g1	CAGCAGAACTCTCACGACCA
ARID1A g2	CAGACACATAGAGGCGATAG

DRG1 g1	GAGCCTTAAGCAGCCCTAAG
DRG1 g2	AGGTATCATTGAAGGTGCCA
CTSL g1	CTGGGGGCCTCATAAAACAG
CTSL g2	CAGTATGTTCAGGATAATGG
UBXN7 g1	GTGGCCGGAATAGATCTGCA
UBXN7 g2	TCAGGTGCAAGTGAAAGTGT
CRSL1 g1	CCTTCCCCGCGCCCGAACAG
CRSL1 g2	TAATCAAATAGCCCAGAACT
SMARCA4 g1	GCAGCAGACAGACGAGTACG
SMARCA4 g2	CTAGGTATGAAGTAGCTCCG
ATP8B1 g1	CTGCAAAAATGACTAAGCCG
ATP8B1 g2	AGTTCCTCAAATCTCTACCC
VPS52 g1	CAATGAACGAGCAACAGCAA
VPS52 g2	TCCGTAACATTGCAGCAAAG
PSIP1 g1	AGATCGAAAACGCAAGCAAG
PSIP1 g2	AAGAGCCGGATAAAAAAGAG

1353

1354 **Table 3. sgRNA sequences used for CRISPRa perturbations**

Gene	sgRNA sequence
CTRL g1	AGCACGTAATGTCCGTGGAT
CTRL g2	CAATCGGCGACGTTTTAAAT
ACE2 g1	AGCCAATATAAAGTTCATCC
ACE2 g2	GTTACATATCTGTCCTCTCC
IFNL2 g1	GGTAAGACACCGGCCACCAG
IFNL2 g2	CACAGCCTCAGGTAAGACAC
PLAGL1/HYMAI g1	CCAAGAGGATGGCTGCGCCG
PLAGL1/HYMAI g2	GCCGTGGGCTTTGCCGCCCG
MUC4 g1	GCTGATGAGAAGCAGAGCAA
MUC4 g2	CTGATGAGAAGCAGAGCAAC
JADE3 g1	CAGCCCGCCAGAAGAACGCG
JADE3 g2	CCCGCCAGAAGAACGCGCGG
MUC21 g1	CCTGGGACGGAATAGAGCAG
MUC21 g2	TAGAGCAGGGGTCAAGAGGA
IL6R g1	GCAACGCAGGAAAACATTTG
IL6R g2	ATCAACAGAACCGGGAGGAA
LY6E g1	GGAGCCGGGGTAGGCCTGGG
LY6E g2	CTATCCCAAGGAGCCGGGGT
LYN g1	GCCTTCAAAGCCCTGCGCGA
LYN g2	AAACACCCAAACCTTGGGCA
CUX1 g1	GGAGGAGTCCGCGTCCTCGG
CUX1 g2	TGAGGAGGAGTCCGCGTCCT
FXYD5 g1	CTGGCTTCAGAGCCCGGGGT
FXYD5 g2	GCATAGTGGTGGGAGAGGGT
LRNF5 g1	CGCACACCCAGCACTGCACG
LRNF5 g2	ACGGGGAGGAAGCAGCACGG
ATAD3B g1	CTATGGCGTCACTGCCCTCG
ATAD3B g2	TTTAGGAGCGTGCTCCGGGG
TEAD3 g1	TCGCGAGGCCGCGGGGTAGG
TEAD3 g2	CGCTCGGGCCGCCTACCCCG
OR1N1 g1	AATGAACTTAAAGGGAGATT
OR1N1 g2	ATGAACTTAAAGGGAGATTT
BHLHA15 g1	CCGCCGGGACACCCGGACCC
BHLHA15 g2	CGGGGTCCGGGTGTCCCGGC
MUC1 g1	AGAGCCCTTGTACCCTACCC
MUC1 g2	CCTTGTACCCTACCCAGGAA

MYRF g1	GAGCGCCGCCTGCAGGAGTC
MYRF g2	AGTCGGGAGCGTGGTGCCCG
MAFK g1	CGCCCTCCTCTCCCGCCCGG
MAFK g2	GGGGATTGCAGGTGCGCGCG
ZNF572 g1	AGGGTTAAGATCAACGAGAG
ZNF572 g2	CTTCTGGTCCAGGACCCTAA
CD44 g1	AGGACACACCCAAGCAAGGG
CD44 g2	TAAGAAGTAGCAGCCCTCCC
ATP4V0A2 g1	GCCAACCAGCGCGAACCCGG
ATP4V0A2 g2	GTTGTCGCCGCACGACGTGG
FBXL19 g1	TTCGTCCTGGAAAGTGGAGG
FBXL19 g2	GCGTTCGTCCTGGAAAGTGG
ZNF703 g1	CAGCTCTCGCCGGGACCCCG
ZNF703 g2	CTGAGGCCGGCTCCATCGGT
SLC6A14 g1	TACCGGAAGGGACTAAAGTG
SLC6A14 g2	GCTACATGTAGGCTTATCTG
TP73 g1	GCGGGGCCAAGGTCTCCTCC
TP73 g2	TGGAGAGGCGGAGCGCCGGG
HNF1B g1	ACCTGGAGAGCAGAAGACCT
HNF1B g2	CGGCTGGATGCAAATGATGG
NFE2 g1	CTGCCCCTTTCGGCCAAGAG
NFE2 g2	GAGGAAACTTGAGCCCGATG
SLC6A19 g1	CTGCAGGGTGCGTCTGCGGA
SLC6A19 g2	CCTGCAGATCTGCTGACGAC

Supplementary Files

This is a list of supplementary files associated with this preprint. Click to download.

- SupplementalFile1allscreens.xlsx
- SupplementalFile2VeroE6thisstudy.xlsx
- SupplementalFile3Calu3Gattinara.xlsx
- SupplementalFile4Calu3Calabrese.xlsx
- SupplementalFile5Caco2Brunello.xlsx